Performance of arm locking in LISA

Kirk McKenzie, Robert E. Spero, and Daniel A. Shaddock*

Jet Propulsion Laboratory, California Institute of Technology, Pasadena, California 91109, USA
(Received 27 July 2009; published 16 November 2009)

For the Laser Interferometer Space Antenna (LISA) to reach its design sensitivity, the coupling of the free-running laser frequency noise to the signal readout must be reduced by more than 14 orders of magnitude. One technique employed to reduce the laser frequency noise will be arm locking, where the laser frequency is locked to the LISA arm length. In this paper we detail an implementation of arm locking. We investigate orbital effects (changing arm lengths and Doppler frequencies), the impact of errors in the Doppler knowledge that can cause pulling of the laser frequency, and the noise limit of arm locking. Laser frequency pulling is examined in two regimes: at lock acquisition and in steady state. The noise performance of arm locking is calculated with the inclusion of the dominant expected noise sources: ultrastable oscillator (clock) noise, spacecraft motion, and shot noise. We find that clock noise and spacecraft motion limit the performance of dual arm locking in the LISA science band. Studying these issues reveals that although dual arm locking [A. Sutton and D. A. Shaddock, Phys. Rev. D **78**, 082001 (2008)] has advantages over single (or common) arm locking in terms of allowing high gain, it has disadvantages in both laser frequency pulling and noise performance. We address this by proposing a modification to the dual arm-locking sensor, a hybrid of common and dual arm-locking sensors. This modified dual arm-locking sensor has the laser frequency pulling characteristics and low-frequency noise coupling of common arm locking, but retains the control system advantages of dual arm locking. We present a detailed design of an arm-locking controller and perform an analysis of the expected performance when used with and without laser prestabilization. We observe that the sensor phase changes beneficially near unity-gain frequencies of the arm-locking controller, allowing a factor of 10 more gain than previously believed, without degrading stability. With a time-delay error of 3 ns (equivalent of 1 m interspacecraft ranging error), time-delay interferometry (TDI) is capable of suppressing $300 \text{ Hz}/\sqrt{\text{Hz}}$ of laser frequency noise to the required level. We show that if no interspacecraft laser links fail, arm locking alone surpasses this noise performance for the entire mission. If one interspacecraft laser link fails, arm locking alone will achieve this performance for all but approximately 1 h per year, when the arm length mismatch of the two remaining arms passes through zero. Therefore, the LISA sensitivity can be realized with arm locking and time-delay interferometry only, without any form of prestabilization.

I. INTRODUCTION

The Laser Interferometer Space Antenna (LISA) [1] is a joint NASA-ESA mission to observe gravitational wave signals of astronomical origin. LISA will consist of three spacecraft arranged in a triangular formation with 5×10^9 m sides (arms). Laser interferometry will be used to sense the spacecraft separation to a precision of $\delta x = 40 \text{ pm}/\sqrt{\text{Hz}}$ increasing as f^{-2} below 3 mHz, giving a strain sensitivity of $h \sim 10^{-20}/\sqrt{\text{Hz}}$. Unlike ground based gravitational wave detectors, which are based on Michelson interferometers with equal arm lengths, the LISA arm lengths vary over time and will be unequal for the majority of the mission. Over the period of a year, the arm lengths will vary by approximately 3% of the total arm length, or by $\pm 76\,500$ km [2]. Given this level of arm length mismatch, there are stringent laser frequency noise requirements: coupling of the free-running frequency noise

of a Nd:YAG laser to the signal output must be reduced by more than 14 orders of magnitude.

The frequency noise requirement is expected to be met using three techniques in unison: (1) prestabilization, where the laser frequency is locked to either the resonance of a Fabry-Perot cavity [3,4], or to a mismatched arm length Mach-Zehnder (MZ) interferometer [5]; (2) arm locking [6–8], a technique based on transferring the stability of the LISA arm length to the laser frequency; and (3) time-delay interferometry (TDI) [9–11], a postprocessing technique that synthesizes interferometers with equal arm lengths by combining phase measurements with appropriate delays.

The initial arm locking proposal by Sheard *et al.* [6] showed that the round-trip propagation delay, $\tau \approx 33$ s, of the LISA measurement scheme did not necessarily limit the arm-locking control system to a low bandwidth, low gain system. This is because instantaneous information of the laser phase noise is obtained via the local oscillator field used in each one-way phase measurement. By careful design of the controller, the arm-locking control system

---

*Also at The Centre for Gravitational Physics, Australian National University, ACT 0200, Australia.

can encompass many interferometer nulls to deliver a high-bandwidth, high gain system over the LISA measurement band.

High-bandwidth arm locking has been demonstrated in hardware [12–14] and analyzed theoretically [8]. Dual arm locking [15], built on the proposal of enhanced arm locking by Herz [16], uses combinations of phase measurements from two arms to increase the frequency of the first null of the sensor from $1/\tau \approx 30$ mHz to $1/(2\Delta\tau) \gtrsim 2$ Hz, where $\Delta\tau$ is the 1/2 difference in light travel round-trip times of the two arms used. Moving the first null to outside the LISA band allows a more aggressive controller design below 2 Hz and eliminates from the LISA science band noise amplification due to the nulls.

Although there have been many studies of arm locking, there has been little analysis of how it would be implemented in LISA, the operation of it, the performance limitations due to noise sources, or the effects associated with the changing arm lengths and Doppler shifts. This paper is intended to provide a detailed study of these issues and to predict the performance limitations of arm locking in LISA. The analysis is performed for a continuous system, though the implementation on LISA will be digital; we expect the difference in performance will be minor. The following issues are analyzed:

(1) The arm-locking measurement architecture. That is, which phase meter signals should be used in the arm-locking sensor.

(2) Laser frequency pulling due to an error in the Doppler frequency estimate. The phase measurements used in arm locking require an estimate of the Doppler frequency to be subtracted. Estimation error causes the laser frequency to ramp, pulled from the starting frequency. Laser frequency pulling occurs both at lock acquisition and throughout the orbit. To prevent significant laser frequency pulling, either the Doppler frequency estimate must be updated regularly or low-frequency filtering should be implemented.

(3) The significant noise sources in arm locking. These are as follows:

(a) Noise of ultrastable oscillators (USO's), or clocks as we call them henceforth, which enters at each phase meter measurement.

(b) Spacecraft motion, which is significantly larger than the proof mass motion and is present in most of the phase measurements.

(c) Shot noise, due to the quantized nature of the electromagnetic field.

These effects are investigated using the common and dual arm-locking sensors [15] and are written in a general formalism applicable to any sensor. We introduce a modification to the dual arm-locking sensor that combines the reduced noise and reduced frequency pulling of common arm locking and the higher gain of dual arm locking. We present a controller design that maximizes frequency noise

suppression, including a factor of 10 more gain than previously assumed [15], while retaining a conservative phase margin. This controller suppresses laser frequency to a level low enough that arm locking and TDI alone, without frequency prestabilization, are adequate for the ultimate sensitivity requirement.

The paper is laid out as follows: In Sec. II the notation used throughout the paper is introduced, and the various possible arm-locking sensors previously published are listed. The detailed study begins in Sec. III by examining which phase meter signals should be used in the arm-locking sensor. In Sec. IV laser frequency pulling is examined at lock acquisition and in steady state. The largest noise sources of arm locking are examined in Sec. V, and written into a general formalism for the noise floor of arm locking in Sec. VI. In Sec. VII the new dual arm-locking sensor is presented. In Sec. VIII we present a design of the arm-locking controller. Finally, in Sec. IX we discuss the performance limitations of arm locking to give a realistic estimate of arm-locking performance in LISA.

II. NOTATION AND SPECTRA

In this section we introduce notation, and write down the arm-locking sensors and the laser frequency noise spectra we shall assume for the rest of the paper.

A. Notation

Figure 1 shows a simplified schematic of the LISA measurement scheme and the signal routing for arm locking. For simplicity, only two of the three spacecraft are drawn and only laser frequency noise is considered. In Sec. VI shot noise, clock noise, and spacecraft motion are added to the calculation. We label the three spacecraft 1, 2, and 3, and take spacecraft 1 to be the central spacecraft of the dual arm-locking configuration. The phase meter output on each spacecraft is given by propagating the laser noise source to the phase meter. To start with, assume that all control loops are open. In the frequency
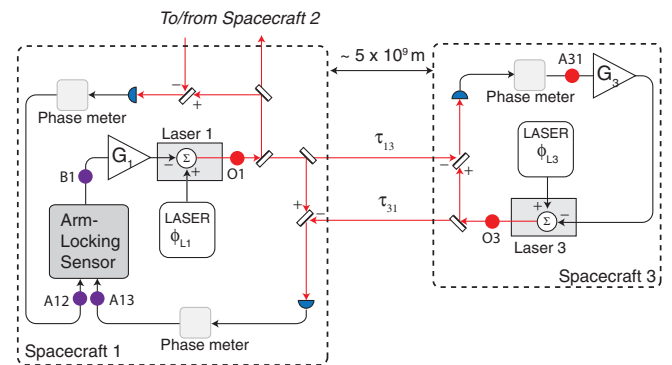

FIG. 1 (color online). Schematic of arm-locking control loop. Laser frequency noise is represented by ϕ_{Lj}, with j representing the number of the local spacecraft.

domain, the phase measured at the output of the phase meter on spacecraft 3, facing spacecraft 1 (represented by the red circle labeled $A31$) is

$$\phi_{A31}(\omega) = \phi_{L3}(\omega) - \phi_{L1}(\omega)e^{-i\omega\tau_{13}}, \quad (1)$$

where $\phi_{Lj}(\omega)$ is the laser phase noise of the laser on the jth spacecraft prearm locking expressed in units of cycles/$\sqrt{\text{Hz}}$, and τ_{13} is the light propagation time between spacecrafts 1 and 3. For simplicity we assume[1] $\tau_{ij} = \tau_{ji}$. If the laser on spacecraft 3 is phase locked to the incoming light, the closed loop phase noise at the output of laser 3 (represented by the red circle labeled $O3$) is

$$\phi_{O3}(\omega) = \frac{\phi_{L3}(\omega)}{1 + G_3(\omega)} + \frac{G_3(\omega)}{1 + G_3(\omega)}\phi_{L1}(\omega)e^{-i\omega\tau_{13}}, \quad (2)$$

where $G_3(\omega)$ is the frequency response of the phase-locking controller on spacecraft 3. With the laser on spacecraft 3 phase locked to the incoming light, but the arm-locking control loop is open [$G_1(\omega) = 0$], the phase at the phase meter output labeled $A13$ on spacecraft 1 is given by

$$\phi_{A13}(\omega) = \phi_{L1}(\omega)P_{13}(\omega) - \frac{\phi_{L3}(\omega)}{1 + G_3(\omega)}e^{-i\omega\tau_{13}}, \quad (3)$$

where $P_{13}(\omega)$ is the frequency response of the 1-3 arm, including the prompt and delayed signals. The calculation of phase $\phi_{A12}(\omega)$ follows a similar argument. The frequency responses of the two arms are

$$P_{13}(\omega) = 1 - \frac{G_3(\omega)}{1 + G_3(\omega)}e^{-i2\omega\tau_{13}},$$
$$P_{12}(\omega) = 1 - \frac{G_2(\omega)}{1 + G_2(\omega)}e^{-i2\omega\tau_{12}}, \quad (4)$$

with $G_2(\omega)$ the controller gain of the phase-locking loop on spacecraft 2. In the high gain transponder limit[2] $G_j(\omega)/(1 + G_j(\omega)) \rightarrow 1$ and $1/(1 + G_j(\omega)) \rightarrow 0$ for $j = 2, 3$, and the frequency responses of the two arms are approximately

$$P_{13}(\omega) \approx 1 - e^{-i2\omega\tau_{13}}, \qquad P_{12}(\omega) \approx 1 - e^{-i2\omega\tau_{12}}, \quad (5)$$

and the phases that enter the arm-locking sensor are

$$\phi_{A13}(\omega) \approx \phi_{L1}(\omega)P_{13}(\omega), \quad (6)$$

$$\phi_{A12}(\omega) \approx \phi_{L1}(\omega)P_{12}(\omega). \quad (7)$$

We adopt the approximations of (5)–(7) in the sequel.

----

[1]In general, the light propagation time to and from each spacecraft will not be equal due to the motion of the constellation.

[2]The phase-locking control loops are expected to have a unity-gain frequency >30 kHz, yielding high gain across the LISA science band.

B. Arm-locking sensors

The phase measurements that enter the arm-locking sensor on the central spacecraft are

$$\Phi_{A1} = \begin{bmatrix} \phi_{A13}(\omega) \\ \phi_{A12}(\omega) \end{bmatrix}. \quad (8)$$

We are interested in the performance of both common and dual arm locking. This is because the modified dual arm-locking sensor, introduced in Sec. VII, is a hybrid of the two. In common arm locking, phase measurements from both arms are simply added. The mapping of the two input signals for common arm locking is given by the vector

$$\mathbf{S}_+ = \begin{bmatrix} 1 & 1 \end{bmatrix}. \quad (9)$$

The open loop noise at the output of the arm-locking sensor (point $B1$ in Fig. 1) is simply

$$\phi_{B1}|_+(\omega) = \mathbf{S}_+\Phi_{A1}. \quad (10)$$

We will be interested in the frequency noise at the laser output with the arm-locking control loop closed. This is the noise at the point $O1$ in Fig. 1. With the arm-locking control loop closed [$G_1(\omega) \neq 0$] the frequency noise at the laser output is given by

$$\phi_{O1}|_+(\omega) = \phi_{L1}(\omega) - \frac{G_1(\omega)P_+(\omega)\phi_{L1}(\omega)}{1 + G_1(\omega)P_+(\omega)}, \quad (11)$$

$$= \frac{\phi_{L1}(\omega)}{1 + G_1(\omega)P_+(\omega)}, \quad (12)$$

where $P_+(\omega) = P_{13}(\omega) + P_{12}(\omega)$ is the frequency response of the common arm-locking sensor,[3] also given in Table I.

For dual arm locking, the signal mapping vector is [15]

$$\mathbf{S}_D = \begin{bmatrix} 1 - \frac{E(\omega)}{i\omega\Delta\tau} & 1 + \frac{E(\omega)}{i\omega\Delta\tau} \end{bmatrix}. \quad (13)$$

The open loop noise at the output of the arm-locking sensor (point $B1$ in Fig. 1) is

$$\phi_{B1}|_D(\omega) = \mathbf{S}_D\Phi_{A1}, \quad (14)$$

and the closed loop output is

$$\phi_{O1}|_D(\omega) = \frac{\phi_{L1}(\omega)}{1 + G_1(\omega)P_D(\omega)}, \quad (15)$$

with $P_D(\omega)$ the frequency response of the dual arm-locking sensor. The signal mapping vectors of, and frequency responses for, single, common, and dual arm locking are contained in Table I. The parameter $E(\omega)$ in the dual arm-locking signal mapping vector is a filter designed to ensure

----

[3]In defining the sensors in this paper we have assumed the high gain transponder limit; thus we use the approximation of $P_{12}(\omega)$ and $P_{12}(\omega)$ given in Eq. (5).

TABLE I.   The signal mapping vector and frequency response of different arm-locking configurations. Here τ_{ij} is the one-way light travel time of the ijth arm, $\bar{\tau}$ is the average round-trip time of the two arms, and $E(\omega)$ is a filter used to combine the common and difference sensors, given in Table II. The parameters $H_+(\omega)$ and $H_-(\omega)$ are defined in Eqs. (70) and (71).

Configuration	Signal mapping	Frequency response
Single	$\mathbf{S}_S = \begin{bmatrix} 1 & 0 \end{bmatrix}$	$P_S(\omega) = 2i\sin(\tau_{ij}\omega)e^{-i\omega\tau_{ij}}$
Common	$\mathbf{S}_+ = \begin{bmatrix} 1 & 1 \end{bmatrix}$	$P_+(\omega) = 2(1 - \cos(\Delta\tau\omega)e^{-i\omega\bar{\tau}})$
Difference	$\mathbf{S}_- = \begin{bmatrix} 1 & -1 \end{bmatrix}$	$P_-(\omega) = -2i\sin(\Delta\tau\omega)e^{-i\omega\bar{\tau}}$
Dual	$\mathbf{S}_D = \begin{bmatrix} 1 - \frac{E(\omega)}{i\omega\Delta\tau} & 1 + \frac{E(\omega)}{i\omega\Delta\tau} \end{bmatrix}$	$P_D(\omega) = P_+(\omega) - \frac{E(\omega)}{i\omega\Delta\tau}P_-(\omega)$
Modified dual	$\mathbf{S}_M = \begin{bmatrix} H_+(\omega) - H_-(\omega) & H_+(\omega) + H_-(\omega) \end{bmatrix}$	$P_M(\omega) = P_+(\omega)H_+(\omega) - P_-(\omega)H_-(\omega)$

stability when the common and difference sensors are combined [15]. The values used in this paper are given in Table II.

The sensors in this paper that contain the addition of the two arms (common, dual, and modified dual) have a frequency response magnitude up to twice that of the single arm-locking sensor. To take account of this factor of 2 difference, we define the controller for any such sensor as $G_1(\omega) = \frac{G_1^*(\omega)}{2}$. For dual arm locking, which has a frequency response of magnitude 2 at $f < 1/2\Delta\tau$, this means that we can design a controller $G_1^*(\omega)$ as if we had

TABLE II.   Parameters of the filter contained in the dual arm-locking sensor. The filter is defined as $E(\omega) = E_1 E_2$.

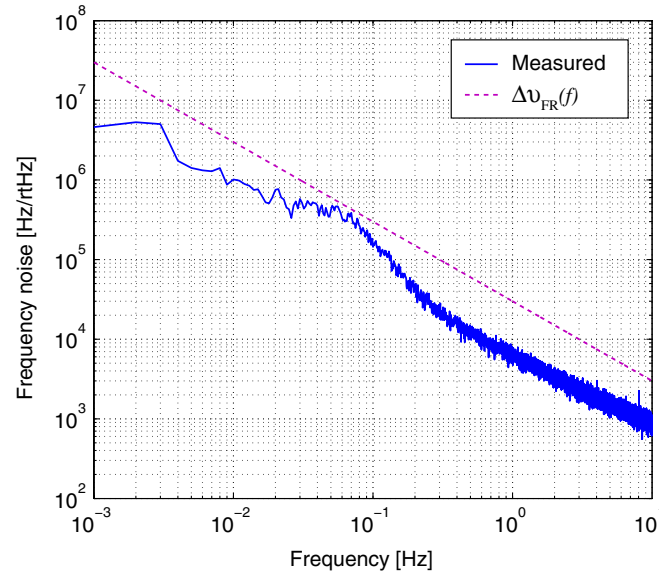| Filter	Zeros (rad/s)	Poles (rad/s)	Gain
E_1		$p_1 = 2\pi \times 0.1394/\Delta\tau$	$g_1 = p_1$
E_2	$z_2 = 2\pi \times 10/\Delta\tau$	$p_2 = 2\pi \times 5/(2\Delta\tau)$	$g_2 = p_2/z_2$

FIG. 2 (color online).   A measurement of the frequency noise between two NPRO Nd:YAG lasers (solid trace), and the assumed free-running laser noise assumed in this paper (dashed trace). The phase of the beat note was measured using the LISA phase meter. The dashed trace is given by Eq. (16).

a sensor with unity magnitude, making the design process more intuitive.

C. Laser frequency noise spectra

The level and shape of the laser frequency noise spectrum is required for a number of calculations in this paper. We use three different initial laser noise levels: free-running laser noise, and laser noise predicted for two types of prestabilization, Fabry-Perot cavity stabilization and Mach-Zehnder stabilization. The corresponding laser frequency noise levels are (square root of power spectral density)

$$\tilde{\nu}_{FR}(f) = 30\,000 \times 1\,\text{Hz}/f\,\frac{\text{Hz}}{\sqrt{\text{Hz}}}, \qquad (16)$$

$$\tilde{\nu}_{MZ}(f) = 800 \times (1 + (2.8\,\text{mHz}/f)^2)\,\frac{\text{Hz}}{\sqrt{\text{Hz}}}, \qquad (17)$$

$$\tilde{\nu}_{FP}(f) = 30 \times (1 + (2.8\,\text{mHz}/f)^2)\,\frac{\text{Hz}}{\sqrt{\text{Hz}}}. \qquad (18)$$

The free-running laser noise level quoted here is conservative. A measurement of the beat between two free-running laser Nd:YAG nonplanar ring oscillator (NPRO) lasers is shown in Fig. 2. These results were taken by interfering two free-running lasers on a beam splitter (both Lightwave model 126), detecting one output of the beam splitter on a photodetector and measuring the resultant phase of the beat note using the LISA phase meter [17]. This measurement is always under $25\,000 \times 1\,\text{Hz}/f\,\text{Hz}/\sqrt{\text{Hz}}$ which, assuming the two lasers have identical noise properties, indicates a free-running laser noise of one laser of less than $18\,000 \times 1\,\text{Hz}/f\,\text{Hz}/\sqrt{\text{Hz}}$.

III. MEASUREMENT ARCHITECTURE FOR ARM LOCKING

The LISA science measurement is performed between proof masses on the local spacecraft and distant spacecraft using the postprocessing technique, TDI. Time-delay interferometry will be implemented on Earth by forming linear combinations of low bandwidth (~ 3 Hz) phase measurements with delays determined by interspacecraft ranging [18]. This process requires five phase measurements on each optical bench (with two optical benches per

spacecraft). These phase measurements are [19] (1) inter-spacecraft measurement, (2) the backlink measurement, (3) the proof mass to optical bench measurement, and (4) and (5), the beat notes of the upper-upper and lower-lower clock sidebands. Time-delay interferometry forms the displacement measurement using the strap-down architecture [20], which combines the interspacecraft measurements, the proof mass to optical bench, and the backlink measurement to remove spacecraft motion. Clock noise in the measurement can be removed using the beat note of clock sidebands [21–25].

Unlike TDI, arm locking requires high-bandwidth signals (~ 20 kHz), in real time, and has significantly less stringent noise requirements than the LISA science measurement. Given the relaxed noise requirements, we assume that arm locking will operate with the most simple measurement architecture—*using only the interspacecraft phase measurements*. A consequence of choosing this measurement architecture is that both clock noise and spacecraft motion will be present in the phase measurements used for arm locking. In Sec. V we see that clock noise and spacecraft motion represent the largest noise sources for arm locking in the science band.

IV. LIMITING LASER FREQUENCY PULLING

The heterodyne frequency of the interspacecraft measurement is set by the Doppler shift of the laser light, due to the relative motion of the spacecraft. The relative velocities in each arm will be up to 18 m/s, corresponding to a Doppler shift of up to 18 MHz [26]. For arm locking to operate stably, this round-trip Doppler frequency must be estimated and subtracted in the phase measurements used in the arm-locking sensor [27]. In the limit of a high gain DC coupled arm-locking control system, an error in the estimated Doppler frequency is compensated for by changing the local laser frequency to maintain the desired beat note frequency. In single arm locking, this frequency change will appear on the light returning from the distant spacecraft 33 s later, necessitating a further change by the local laser frequency to maintain the desired beat note frequency. The closed loop master laser frequency, ν_{CL}, will be changed by the error in the Doppler frequency, ν_{DE}, each round-trip, or an average rate of

$$\frac{\delta\nu_{\mathrm{CL}}}{\delta t} = \nu_{\mathrm{DE}}\frac{c}{2L} \ [\mathrm{Hz/s}]. \tag{19}$$

For example, if the Doppler frequency can be estimated to 100 kHz, the laser frequency will be forced to change by 1 GHz in 4 days. Such large pulling of the laser frequency is undesirable, as it could drive the master laser through a mode-hop region, compromising instrument sensitivity. The other lasers in the constellation are also at risk of being pulled into a mode-hop region as they will be locked to the master laser frequency. Additionally, ramping of

laser frequency combined with scattered light sources can couple noise into the science band [28].

We study frequency pulling in two regimes: (1) in steady state operation, and (2) at lock acquisition. At lock acquisition, the laser frequency can be pulled significantly by an error in the initial Doppler frequency estimate and also in the time derivatives of the Doppler frequency.

The solution to this problem explored in detail here is to add high pass filters to the arm-locking control loop at a frequency below the LISA science band. This low-frequency modification to the controller limits the laser frequency pulling at lock acquisition and allows indefinite operation of the arm-locking control system with an acceptable level of pulling. An alternate and closely related solution presented by Gath [29], is based on a DC coupled controller with an additional control loop operating at low frequencies to limit the amplitude of the controller signal at these frequencies. This active solution may have precision advantages in implementation.

The arm-locking control system operates as follows: before arm locking is engaged, measurements of the Doppler frequency and the Doppler rate (the first time derivative of the Doppler frequency) will be made (Appendix A) and subtracted from the phase meter measurement. After the control loop is closed the error in the Doppler frequency measurement will cause the laser frequency to ramp at a rate proportional to the product of the error and the step response of the controller. While locked, the Doppler frequency estimate will not need to be updated. The arm-locking control loop will be unlocked and relocked periodically to perform mission tasks, such as to change the heterodyne frequencies [26]. At these times the Doppler frequency and its time derivatives will be known very accurately (as many weeks or months of data can be averaged to measure it) and the impulse to laser frequency will be much smaller than the first time arm locking is engaged.

In the following sections we describe the extent of the frequency pulling and how to limit it. We shall examine the lock acquisition and steady state operation regimes separately. We start by calculating the frequency response of the Doppler frequency error into the stabilized laser frequency. These results are considered in the controller design process presented in Sec. VIII, where we show that with the frequency pulling limited to an acceptable level, high gain can be achieved across the LISA science band.

A. Frequency response to Doppler frequency error

1. Single arm locking

The block diagram in Fig. 3 shows where the Doppler frequency error enters the single arm-locking control loop. Here ν_{OL} is the initial (open loop) laser frequency, ν_{CL} the stabilized (closed loop) laser frequency, and $P_S(\omega)$ and $G_1(\omega)$ are the frequency responses of the single-arm sensor

FIG. 3. Block diagram of the single arm-locking control system showing where the Doppler frequency error ν_{DE} enters the control loop. $P_S(\omega)$ and $G_1(\omega)$ are frequency responses of the sensor and controller, respectively. The laser frequency with the control loop open and closed are ν_{OL} and ν_{CL}.

and controller, respectively. The Doppler frequency error enters the phase measurement in the phase meter, where an estimate of the Doppler frequency is subtracted from the phase measurement. The closed loop frequency will be pulled by

$$\nu_{CL}|_S = \frac{-G_1(\omega)\nu_{DE}}{1 + G_1(\omega)P_S(\omega)}. \tag{20}$$

The frequency response of the Doppler frequency error to the stabilized laser frequency for single arm locking is simply

$$Y_S(\omega) = \frac{\nu_{CL}|_S}{\nu_{DE}} = \frac{-G_1(\omega)}{1 + G_1(\omega)P_S(\omega)}. \tag{21}$$

The frequency pulling due to error in the Doppler frequency can be examined in the extreme cases of low and high loop gain. At high gain,

$$Y_S(\omega) \sim \frac{1}{P_S(\omega)} \qquad [\text{for } G_1(\omega)P_S(\omega) \gg 1], \tag{22}$$

which, as $P_S(\omega) \approx i\omega\tau$ at low frequencies ($f \lesssim 1$ mHz), gives the constant-rate frequency pulling described in Eq. (19). At low gain,

$$Y_S(\omega) \sim G_1(\omega) \qquad [\text{for } G_1(\omega)P_S(\omega) \ll 1]. \tag{23}$$

This equation shows that for an AC coupled control loop the Doppler error is multiplied by the low-frequency gain.

2. Common and dual arm locking

When phase measurements from two arms are used to create the arm-locking sensor the analysis becomes more complex. Figure 4 shows the block diagram for a two signal arm-locking control loop, such as is used in common or dual arm locking. Common arm locking would use only the signal paths with solid lines, whereas dual arm locking uses both solid and dashed lines. There are two errors in the Doppler frequency, one enters at each phase meter: ν_{DE12} and ν_{DE13}. The way the Doppler frequency errors enter the control loop with these sensors is less intuitive than in the single arm-locking case. The Doppler frequency error is

FIG. 4. Block diagram of the common or dual arm-locking control system. Common arm locking would use only the signal paths with solid lines, whereas dual arm locking uses both solid and dashed lines. The Doppler frequency errors that enter at the two phase meters are labeled ν_{DE12} and ν_{DE13}. $P_{12}(\omega)$ and $P_{13}(\omega)$ are the single-arm frequency responses.

added after the individual arm frequency responses and before the combination of the phase measurements to form the common or dual arm-locking sensors.

For common arm locking, the closed loop laser frequency driven by the Doppler frequency error is

$$\nu_{CL}|_+ = \frac{-G_1(\omega)(\nu_{DE12} + \nu_{DE13})}{1 + G_1(\omega)(P_{12}(\omega) + P_{13}(\omega))} \tag{24}$$

$$= \frac{-G_1(\omega)\mathbf{S}_+\mathbf{V}_{DE}}{1 + G_1(\omega)P_+(\omega)}, \tag{25}$$

where

$$\mathbf{V}_{DE} = [\begin{array}{cc} \nu_{DE12} & \nu_{DE13} \end{array}]. \tag{26}$$

For common arm locking, the frequency pulling is caused by the sum of the Doppler frequency errors, $\nu_{DE+} = \nu_{DE12} + \nu_{DE13}$. The relevant frequency response is

$$Y_+(\omega) = \frac{\nu_{CL}|_+}{\nu_{DE+}} = \frac{-G_1(\omega)}{1 + G_1(\omega)P_+(\omega)}. \tag{27}$$

The closed loop laser frequency driven by the Doppler frequency error in dual arm locking can be given in a similar form to Eq. (25) by replacing the signal mapping vector and frequency response

$$\nu_{CL}|_D = \frac{-G_1(\omega)\mathbf{S}_D\mathbf{V}_{DE}}{1 + G_1(\omega)P_D(\omega)}. \tag{28}$$

There are two relevant frequency responses to Doppler frequency errors in dual arm locking: due to the sum and the difference in the Doppler frequency errors

$$Y_D^{(+)}(\omega) = \frac{\partial \nu_{CL}|_D}{\partial \nu_{DE+}} = \frac{-G_1(\omega)}{1 + G_1(\omega)P_D(\omega)}, \tag{29}$$

$$Y_D^{(-)}(\omega) = \frac{\partial \nu_{\text{CL}}|_D}{\partial \nu_{\text{DE}-}} = \frac{-G_1(\omega)E(\omega)}{i\omega\Delta\tau(1 + G_1(\omega)P_D(\omega))}, \quad (30)$$

where $\nu_{\text{DE}-} = \nu_{\text{DE}12} - \nu_{\text{DE}13}$. Because of the additional filtering in the difference path of the dual arm-locking sensor, $Y_D^{(-)}(\omega)$ is inversely proportional to $\omega\Delta\tau$, causing it to dominate the frequency pulling in dual arm locking.

B. Doppler frequency error

We now consider what the Doppler frequency error will be. There will be an error associated with the initial estimate of the Doppler frequency. Also, because the Doppler frequency estimate will not be updated while arm locking is operating (to prevent adding noise in the science band), there will be an error due to the Doppler frequency changing throughout the year. Thus, the Doppler frequency error must be written as a function of time. The Doppler frequency error in the ij arm in the time domain is

$$\nu_{\text{DE}ij}(t) = \nu_{0ij} + \int_0^t \gamma_{ij}(t)dt + \int_0^t \int_0^{t'} \alpha_{ij}(t)dt'dt$$
$$+ \text{(higher order terms)}, \quad (31)$$

where ν_{0ij} is the initial error in Doppler frequency, $\gamma_{ij}(t)$ is the error in the Doppler rate (the first time derivative of the Doppler frequency), and $\alpha_{ij}(t)$ is the error in the second time derivative of the Doppler frequency. We neglect higher order time derivatives of the Doppler frequency because they are sufficiently small.

C. Doppler frequency error at lock acquisition

The analysis in this section is restricted to the study of transients that occur at lock acquisition. We shall design the controller such that the transients will occur over a period of a few days. Over this period the terms $\gamma_{ij}(t)$ and $\alpha_{ij}(t)$ will change little, and for simplicity we shall approximate these terms as constants equal to their initial errors. The Doppler error as a function of time is then

$$\nu_{\text{DE}ij}(t) \approx \nu_{0ij} + \gamma_{0ij}t + \frac{\alpha_{0ij}t^2}{2}, \quad (32)$$

with the initial errors in the Doppler rate and change in the Doppler rate given by γ_{0ij} and α_{0ij}.

In the frequency domain, the Doppler error at lock acquisition is

$$\nu_{\text{DE}ij} \approx \nu_{0ij} + \frac{\gamma_{0ij}}{i\omega} - \frac{\alpha_{0ij}}{2\omega^2}. \quad (33)$$

Because we are interested in common and dual arm-locking configurations, we write

$$\nu_{\text{DE}+} = \nu_{0+} + \frac{\gamma_{0+}}{i\omega} - \frac{\alpha_{0+}}{2\omega^2}, \quad (34)$$

$$\nu_{\text{DE}-} = \nu_{0-} + \frac{\gamma_{0-}}{i\omega} - \frac{\alpha_{0-}}{2\omega^2}, \quad (35)$$

where $\nu_{0\pm} = \nu_{012} \pm \nu_{013}$, and similarly $\gamma_{0\pm} = \gamma_{012} \pm \gamma_{013}$ and $\alpha_{0\pm} = \alpha_{012} \pm \alpha_{013}$.

At lock acquisition, the closed loop laser frequency driven by the Doppler error in common arm locking can be found using Eqs. (27) and (34),

$$\nu_{\text{CL}}|_{0+} = \frac{-G_1(\omega)}{1 + G_1(\omega)P_+(\omega)}\left(\nu_{0+} + \frac{\gamma_{0+}}{i\omega} - \frac{\alpha_{0+}}{2\omega^2}\right). \quad (36)$$

The frequency responses to the error in each term in Eq. (36) written separately are

$$\mathcal{V}_+(\omega) = \frac{-G_1(\omega)}{1 + G_1(\omega)P_+(\omega)}, \quad (37)$$

$$\mathcal{G}_+(\omega) = \frac{-G_1(\omega)}{i\omega(1 + G_1(\omega)P_+(\omega))}, \quad (38)$$

$$\mathcal{A}_+(\omega) = \frac{G_1(\omega)}{2\omega^2(1 + G_1(\omega)P_+(\omega))}. \quad (39)$$

These equations show the error in the initial Doppler rate, γ_{0+} and change in Doppler rate, α_{0+} are integrated over time and as such they can cause significant pulling.

To limit pulling due to ν_{0+}, the control loop must be AC coupled. The lower unity-gain frequency can be determined from the maximum allowable pulling and the error in the Doppler frequency. At the unity-gain frequency,

$$|G_1(\omega_{\text{AC}})P_+(\omega_{\text{AC}})| = 1. \quad (40)$$

At frequencies well below $1/\bar{\tau}$, with $\bar{\tau}$ the average round-trip light travel time of the two arms, the common arm sensor can be well approximated by

$$P_+(\omega)|_{f<0.1 \text{ mHz}} \approx i2\omega\bar{\tau}. \quad (41)$$

If the controller gain is flat at low frequencies, the response is rolled off purely by the arm response, and the unity-gain frequency and the low-frequency gain are by

$$|G_1^*(\omega_{\text{AC}})| = |G_{1\nu}| = \frac{1}{\omega_{\text{AC}}\bar{\tau}}, \quad (42)$$

where we have substituted $G_1^*(\omega) = 2G_1(\omega)$. This gain gives the factor of amplification of the Doppler knowledge error. Equation (42) can be rearranged to obtain the AC coupling frequency for a given low-frequency gain

$$f_{\text{AC}}|_\nu \geq \frac{1}{2\pi\bar{\tau}|G_{1\nu}|}. \quad (43)$$

This result sets the lower bound on the unity-gain frequency based on the allowable gain of the Doppler frequency error. To give maximum gain, we set the lower unity-gain frequency as low as possible, for example, if we allow $|G_{1\nu}| = 1000$, then $f_{\text{AC}} \geq 4.8 \times 10^{-6}$ Hz. To limit pulling due to γ_{0+} and α_{0+}, further constraints are required.

At lock acquisition, the frequency responses to Doppler errors in dual arm locking can be calculated following a similar method. Using Eqs. (29) and (34) the frequency responses for the common path of dual arm locking are

$$\mathcal{V}_D^{(+)}(\omega) = \frac{-G_1(\omega)}{1 + G_1(\omega)P_D(\omega)}, \tag{44}$$

$$\mathcal{G}_D^{(+)}(\omega) = \frac{-G_1(\omega)}{i\omega(1 + G_1(\omega)P_D(\omega))}, \tag{45}$$

$$\mathcal{A}_D^{(+)}(\omega) = \frac{G_1(\omega)}{2\omega^2(1 + G_1(\omega)P_D(\omega))}. \tag{46}$$

The frequency responses for the difference path can be found using Eqs. (30) and (35),

$$\mathcal{V}_D^{(-)}(\omega) = \frac{-G_1(\omega)E(\omega)}{i\omega\Delta\tau(1 + G_1(\omega)P_D(\omega))}, \tag{47}$$

$$\mathcal{G}_D^{(-)}(\omega) = \frac{G_1(\omega)E(\omega)}{\omega^2\Delta\tau(1 + G_1(\omega)P_D(\omega))}, \tag{48}$$

$$\mathcal{A}_D^{(-)}(\omega) = \frac{G_1(\omega)E(\omega)}{i2\omega^3\Delta\tau(1 + G_1(\omega)P_D(\omega))}. \tag{49}$$

A comparison of the frequency responses to common and differential Doppler frequency errors in dual arm locking again reveals that it is the differential Doppler frequency errors which will dominate the frequency pulling at start-up. This is because the differential path response has an extra zero at DC and is inversely proportional to $\Delta\tau$.

D. Laser frequency pulling at lock acquisition

We now have the tools needed to examine the frequency pulling in steady state and at lock acquisition. The magnitude of the pulling at lock acquisition depends on the sensor used, the controller design, and the Doppler frequency estimate. The estimate is made by simply observing the beat note frequency between the incoming and outgoing fields prior to switching arm locking on (Appendix A). In this section we determine the pulling that would occur for both common and dual arm locking at lock acquisition. We shall use the low-frequency part of the controller in Sec. VIII, which was designed to provide sufficient gain over the LISA science band to suppress free-running laser frequency noise to below the expected TDI capability and to limit laser frequency pulling. This design has gain less than unity at $f < 4.8$ μHz, implemented with a series of 4 high pass filters. Further details can be found in Appendix B. Although this controller was not designed specifically for these sensors, the calculation gives both an estimate of pulling that can be expected with each sensor, and a comparison of the two sensors. We calculate the frequency pulling that would occur with

Doppler frequency estimates with $T = 200$ s averaging, as part of arm-locking initialization.

1. Common arm locking

The accuracy of the Doppler frequency estimation needed for common arm locking depends on $\bar{\tau}$, the average arm length. Estimation errors for two assumptions of the laser frequency noise—free-running lasers and Mach-Zehnder prestabilization—are given in Table III, with details in Appendix A. In the case of free-running laser noise, the estimates of γ_{0+} and α_{0+} have an error larger than the maximum value determined by the orbital motion (Appendix C). Thus we do not use the laser measurement of these quantities; rather we estimate them to be zero. With prestabilization the error in the measurement of α_{0+} is larger than its maximum value and thus we estimate it to be zero.

Frequency pulling during lock acquisition is determined by the step response of the control system. The step response follows from the closed loop control system $\nu_{CL}(s)$ according to

$$\nu_{\text{step}}(t) = \mathcal{L}^{-1}\left(\frac{\nu_{CL}(s)}{s}\right), \tag{50}$$

where $s = i\omega$ and $\mathcal{L}^{-1}$ is the inverse Laplace transform operator. Step responses from the error in the three Doppler derivatives are plotted in Fig. 5, for both free-running and prestabilized lasers. The small stairstep pattern at the start of acquisition has amplitude $\nu_{0+}/2$ and period $\bar{\tau}$. The maximum pulling from the errors in all the derivatives of ν_{0+} is 460 and 90 MHz, for the respective cases of free-running and prestabilized lasers.

TABLE III. Initial errors in the common and differential components of Doppler frequency, ν_{0+}, ν_{0-}, Doppler rate, γ_{0+}, γ_{0-}, and second time derivative of Doppler frequency, α_{0+}, α_{0-}, for $T = 200$ s averaging (Appendix A). The columns free-running laser and Mach-Zehnder refer to the initial laser noise spectrum, given by Eqs. (16) and (17), respectively. The numbers with * are the values of the Doppler rate and change in Doppler rate at the nominal start of the mission; the measurement of these parameters with 200 s averaging yields errors larger than the mean values. For the differential Doppler frequency estimates and time derivatives we have taken $\Delta\tau = 0.123$ s.

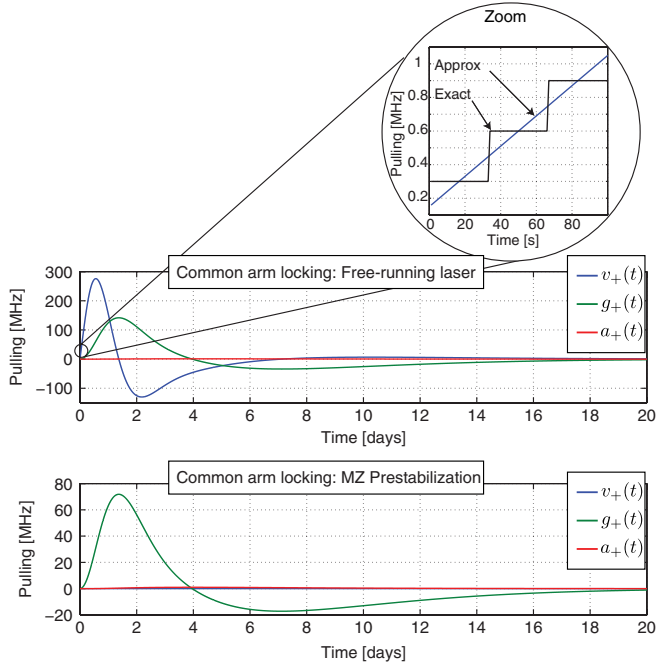| Parameter	Free-running laser	Mach-Zehnder	Units
ν_{0+}	6.0×10^5	45	Hz
ν_{0-}	2.3×10^3	0.51	Hz
γ_{0+}	-4.3^*	2.2	Hz/s
γ_{0-}	1.2^*	0.02	Hz/s
α_{0+}	-0.37^*	-0.37^*	μHz/s^2
α_{0-}	1.0^*	1.0^*	μHz/s^2

FIG. 5 (color online). Step response of the different drivers of Doppler frequency error for common arm locking with Doppler frequency estimate errors with 200 s averaging made with free-running laser noise (top plot), and prestabilized laser noise (lower plot).

2. Dual arm locking

The error in Doppler estimation for dual arm locking is computed the same as in common arm locking, except the relevant delay is $\Delta \tau = 0.123$ s, corresponding to the arm length mismatch of the 12-13 arm combination at the start of the mission. This smaller delay results in smaller error $\nu_{0-} \ll \nu_{0+}$, but larger pulling. As with common arm locking, when the measurement errors in γ_{0-} and α_{0-} are larger than the maximum values taken from the orbits, they are estimated as zero. The estimation errors are tabulated in Table III and the step responses are plotted in Fig. 6. The maximum pulling with estimation based on free-running lasers is 13 GHz, unsuitably large for Nd: YAG lasers that have a typical mode-hop free range of approximately 10 GHz. With prestabilization, the pulling is dominated by the α_{0-} term, with a peak-to-peak value of 250 MHz.

E. Laser frequency pulling in steady state

We now consider frequency pulling in steady state, long after lock acquisition. In steady state operation the pulling will be driven by the change in Doppler frequency which occurs as the constellation orbits the Sun. We determine the pulling in the time domain using a model of the Doppler frequencies over the mission shown in Appendix C.
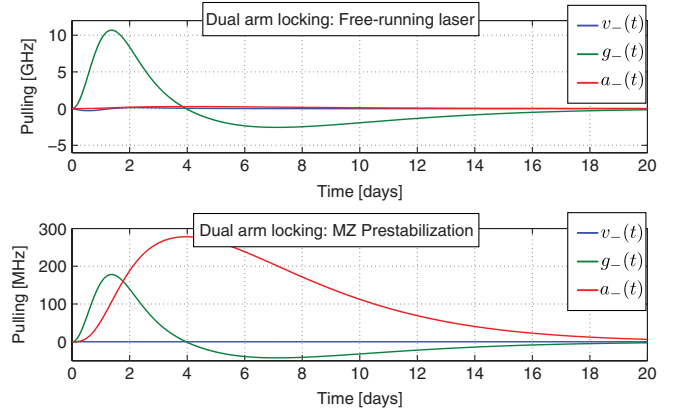
FIG. 6 (color online). Step response of the different drivers of Doppler frequency error for dual arm locking with Doppler frequency estimate errors with 200 s averaging, made with free-running laser noise (top plot) and prestabilized laser noise (lower plot).

1. Common arm locking

The laser frequency pulling in steady state for common arm locking is given by the convolution of the $y_+(t)$, the inverse Laplace transform of $Y_+(\omega)$, and the common Doppler frequency,

$$\nu_{\mathrm{CL}}(t) = y_+(t) * \Delta_+(t), \qquad (51)$$

where $*$ is the convolution operator and $\Delta_+(t)$ is the common Doppler shift in the two arms used in common or dual arm locking shown in Fig. 35. The resulting pulling of the laser is shown in the upper plot of Fig. 7. It can be seen that the laser frequency pulling with the controller designed in Sec. VIII is very modest, less than 8 MHz peak to peak while operating in steady state. The pulling is independent of the laser frequency noise as no Doppler frequency estimates are used and will be an insignificant
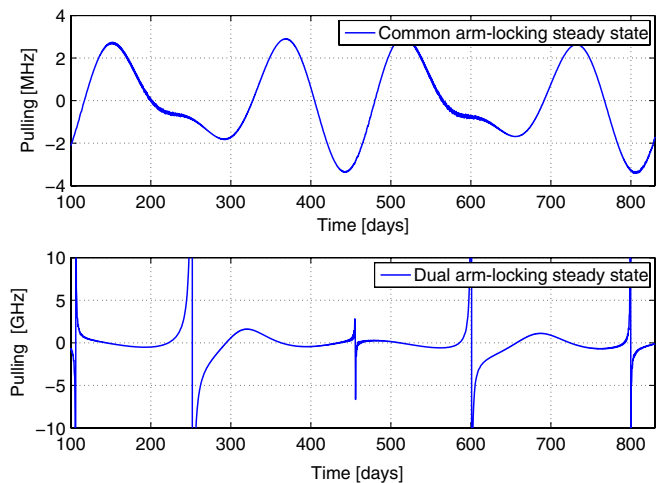
FIG. 7 (color online). The steady state laser frequency pulling of common arm locking (upper plot) and dual arm locking (lower plot).

change compared to the laser frequency drift over this period.

2. Dual arm locking

The laser frequency pulling in steady state for dual arm locking is given by

$$\nu_{CL}(t) = y_D^{(+)}(t) * \Delta_+(t) + y_D^{(-)}(t) * \Delta_-(t), \qquad (52)$$

where $\Delta_-(t)$ is the differential Doppler shift of the two arms used by dual arm locking and $y_D^{(+)}(t)$ and $y_D^{(-)}(t)$ are the inverse Laplace transforms of $Y_D^{(+)}(\omega)$ and $Y_D^{(-)}(\omega)$, respectively. The $y_D^{(-)}(t)$ term in Eq. (52) is inversely proportional to the arm length mismatch, which changes significantly throughout the year, dominating the pulling in dual arm locking. The expected pulling for dual arm locking is shown in the lower plot of Fig. 7. This shows unsustainably large pulling of greater than 10 GHz. The pulling which occurs when the arm length mismatch approaches zero becomes rapid and it is unlikely that the lasers could follow this. Also, the time that the frequency pulling is unsustainably large would also be a concern. For example, when the difference in the 12-13 arm passes though zero, the pulling is above 2 GHz for 35 days. If all three arms are available, the central spacecraft in the dual arm-locking sensor can be switched around to prevent the arm length mismatch going to zero. In this case the pulling would be reduced.

F. Discussion of pulling in common and dual arm locking

While maintaining large laser frequency noise suppression over the LISA science band (using the controller designed in Sec. VIII), the laser frequency pulling caused by the Doppler frequency errors in common arm locking are relatively modest and do not pose a significant threat of driving the lasers into a mode-hop region. At lock acquisition, with a measurement of the Doppler frequency with 200 s of averaging, the laser frequency pulling will be less than 460 MHz, if the lasers are free running, or less than 90 MHz if using Mach-Zehnder–type prestabilization. This will be further reduced if Fabry-Perot prestabilization is selected. In steady state, the laser frequency pulling is expected to be less than 10 MHz peak to peak, insignificant compared to the drift of a laser frequency over a similar period.

In contrast, in the form presented in Ref. [15], dual arm locking would have larger pulling, posing a significant threat of driving the lasers into a mode-hop region, and also of coupling in noise from scattered light sources into the science band. At lock acquisition, with a measurement of the Doppler frequency with 200 s of averaging, the laser frequency pulling will be approximately 13 GHz, if the lasers are free running, or approximately 250 MHz if using prestabilization. While 250 MHz of pulling at lock acquis-

ition poses only a small threat of pulling the lasers into a mode-hop region, the laser frequency pulling of dual arm locking in steady state is unsustainable. The laser frequency pulling in steady state is dependent on the arm length mismatch, which passes through zero twice per year for each pair of arms. Thus the viability of dual arm locking in the form presented in Ref. [15] would depend critically on the availability of all interspacecraft laser links. If all laser links were available, the pulling could be reduced by switching the central spacecraft when the arm length mismatch becomes small.

The laser frequency pulling in dual arm locking can be reduced in three ways: (1) reduce the low-frequency gain of the controller, which sacrifices the frequency noise suppression in the science band, (2) implement a scheme to continuously update the Doppler frequency estimate, which would have to be done with a view to not adding noise in the science band or, the solution we explore here, (3) create a modified dual arm-locking sensor, a hybrid common dual arm-locking sensor designed in Sec. VII. This sensor has the frequency pulling of common arm locking, but maintains other control system advantages of dual arm locking.

V. NOISE SOURCES IN ARM LOCKING

Significant noise sources in the arm-locking control system are clock noise, spacecraft motion, and shot noise. These noise sources are common to all arm-locking configurations (e.g. single, common, and dual). We develop a general formalism applicable to all arm-locking configurations. First though, an overview and approximate amplitude of each of these noise sources is given.

A. Clock noise

The phase of the photodetector signal is determined by comparing it to an onboard clock (i.e. USO) signal. Consequently, the noise of the clock signal contributes an error in the phase measurement that enters at the phase meter. The amplitude of the clock noise added to the phase measurement depends on the fractional frequency noise of the clock and scales linearly with heterodyne beat note frequency, Δ_{ij} (in units of Hz). The clock noise added at the ith spacecraft, when measuring the incoming light from the jth spacecraft, is given by

$$\phi_{Cij}(f) = \Delta_{ij}C_i(f) \qquad [\text{cycles}/\sqrt{\text{Hz}}], \qquad (53)$$

where $C_i(f)$ is the clock phase noise normalized to a 1 Hz clock frequency, given by

$$C_i(f) = \frac{\tilde{y}_i(f)}{2\pi f} \qquad [\text{cycles}/\text{Hz}\sqrt{\text{Hz}}], \qquad (54)$$

and $\tilde{y}(f)$ is the fractional frequency fluctuations of the clock. The amplitude and frequency dependence of $\tilde{y}(f)$ is dependent on the type of clock and operational environ-

ment; we use $\tilde{y}(f) = 2.4 \times 10^{-12}/\sqrt{f} \; 1/\sqrt{\text{Hz}}$, corresponding to an assumption of the clock stability in LISA [29].

Clock noise is correlated for measurements on each spacecraft. Thus, clock noise that enters phase meter signals on the central spacecraft can add or subtract coherently with common or dual arm locking.

B. Spacecraft motion

To minimize the disturbances of the space environment on the measurement the spacecraft will fly *drag free* around the local proof masses [1]. This means the location of the spacecraft relative to the proof mass is sensed and controlled to follow the proof mass. Along the axis which the science measurement is made, the spacecraft follows the proof mass with an error of approximately $\Delta\tilde{X} = 2.5 \times \sqrt{1 + (f/0.3 \text{ Hz})^4} \text{ nm}/\sqrt{\text{Hz}}$ [29]. The interspacecraft phase measurements will contain this jitter. Even with this spacecraft motion, the arms represent an excellent frequency reference, as the fractional length stability is still small given the very long arm length. Because dual arm locking utilizes the fractional stability of the arm length mismatch of two arms, the fractional stability is degraded accordingly. Although it is possible to subtract this motion in real time using the same optical measurements as the LISA science measurement, this adds complexity and, as we show in Sec. VI, the noise performance of arm locking is limited by spacecraft motion for only short periods, twice per year.

If the ith spacecraft moves by an amount of $\Delta\tilde{X}_{ij}(f)$ in the direction of the jth spacecraft, the associated phase shift of the laser field traveling from spacecraft i to spacecraft j is[4]

$$\phi_{Xij}(f) = \frac{\Delta\tilde{X}_{ij}(f)}{\lambda} \qquad [\text{cycles}/\sqrt{\text{Hz}}], \qquad (55)$$

where λ is the laser wavelength. Note that in the propagation between the ith and jth spacecraft the laser field will pick up phase noise due to the motion of both spacecraft.

C. Shot noise

Shot noise is a phase error due to the quantization of the electromagnetic field. The phase error of shot noise is inversely proportional to the square root of the optical power received from the distant spacecraft. Here, we model shot noise as phase error added at the photoreciever. Shot noise is given by [1]

$$\phi_{Sij} = \left(\frac{\hbar c}{2\pi} \frac{1}{\lambda P_d}\right)^{1/2} \qquad [\text{cycles}/\sqrt{\text{Hz}}], \qquad (56)$$

---

[4]The spacecraft motion on the central spacecraft will be correlated in the two arms to some extent. We expect the correlation to be small and neglect it here.

where λ is the laser wavelength and P_d is the optical power received from the distant spacecraft. Shot noise at each ij phase measurement is independent and uncorrelated.

VI. QUANTIFYING THE NOISE PERFORMANCE OF ARM LOCKING

A. Calculation of noise in arm locking

In this section we calculate the noise coupling into the arm-locking control system, building on the calculation in Sec. II. The schematic in Fig. 8 indicates where all three noise sources described in Sec. V enter the phase measurements. The phase meter output can be written down in a similar fashion to Sec. II, by propagating each noise source to the phase meter. Again, to start with, we assume that all control loops are open. The phase measured at the phase meter on spacecraft 3, facing spacecraft 1 (represented by the red circle labeled $A31$) is given by

$$\phi_{A31}(\omega) = \phi_{L3}(\omega) - \phi_{L1}(\omega)e^{-i\omega\tau_{13}} - \phi_{X13}(\omega)e^{-i\omega\tau_{13}}$$
$$- \phi_{X31}(\omega) + \phi_{S31}(\omega) + \phi_{C31}(\omega), \qquad (57)$$

where ϕ_{Lj} is the laser phase noise of the laser on the jth spacecraft prearm locking. If the laser on spacecraft 3 is phase locked to the incoming light, the closed loop phase noise at the output of laser 3 (represented by the red circle labeled $O3$) is

$$\phi_{O3}(\omega) = \frac{\phi_{L3}(\omega)}{1 + G_3(\omega)} + \frac{G_3(\omega)}{1 + G_3(\omega)}(\phi_{L1}(\omega)e^{-i\omega\tau_{13}}$$
$$+ \phi_{X13}(\omega)e^{-i\omega\tau_{13}} + \phi_{X31}(\omega)$$
$$- \phi_{S31}(\omega) - \phi_{C31}(\omega)), \qquad (58)$$

where $G_3(\omega)$ is the frequency response of the phase-locking controller on spacecraft 3. With the laser on spacecraft 3 phase locked to the incoming light [$G_3(\omega) \gg 1$], but the arm-locking control loop open [$G_1(\omega) = 0$], the phase at the phase meter output on spacecraft 1 is given by

$$\phi_{A13}(\omega) \approx \phi_{L1}(\omega)P_{13}(\omega) - \phi_{X13}(\omega)(1 + e^{-i2\omega\tau_{13}})$$
$$- 2\phi_{X31}(\omega)e^{-i\omega\tau_{13}} + \phi_{S13}(\omega)$$
$$+ \phi_{S31}(\omega)e^{-i\omega\tau_{13}} + \phi_{C13}(\omega)$$
$$+ \phi_{C31}(\omega)e^{-i\omega\tau_{13}}, \qquad (59)$$

where successive terms represent laser phase noise, motion of the spacecraft, shot noise, and clock noise. Similarly, the phase at point $A12$ is

$$\phi_{A12}(\omega) \approx \phi_{L1}(\omega)P_{12}(\omega) - \phi_{X12}(\omega)(1 + e^{-i2\omega\tau_{12}})$$
$$- 2\phi_{X21}(\omega)e^{-i\omega\tau_{12}} + \phi_{S12}(\omega)$$
$$+ \phi_{S21}(\omega)e^{-i\omega\tau_{12}} + \phi_{C12}(\omega)$$
$$+ \phi_{C21}(\omega)e^{-i\omega\tau_{12}}. \qquad (60)$$

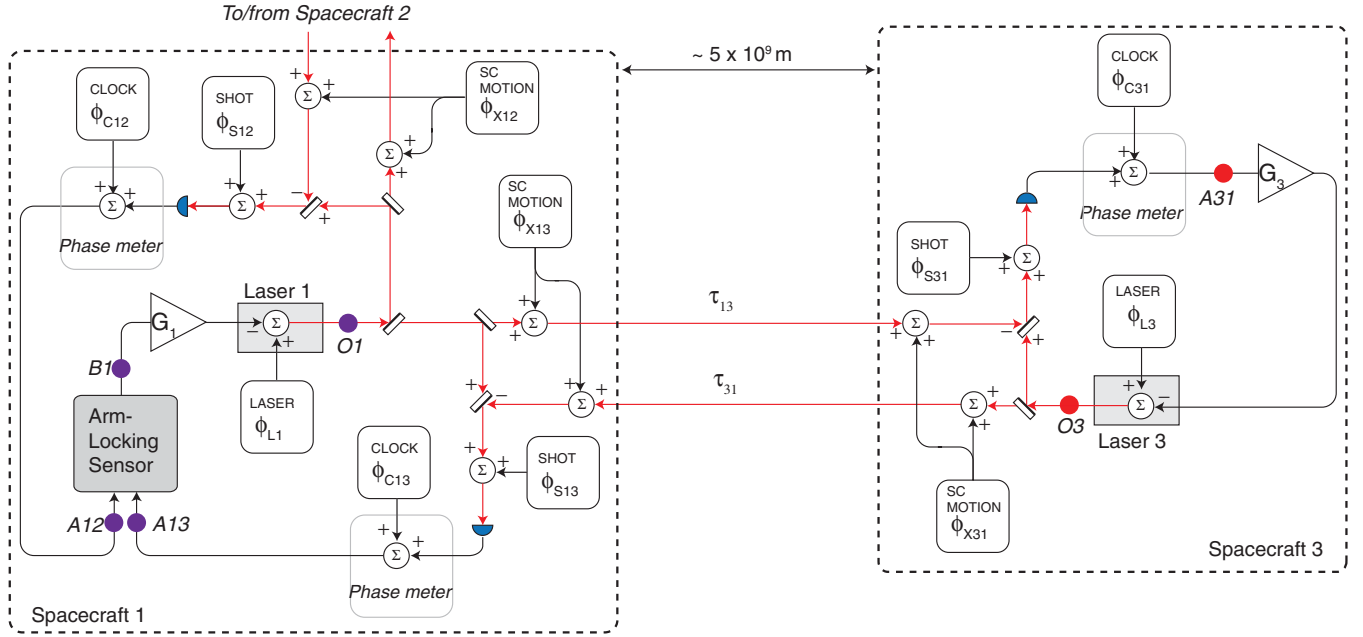The phase measurements that enter the arm-locking sensor

FIG. 8 (color online). Schematic of dual arm-locking control loop showing where the different noise sources enter the system. These are laser frequency noise, ϕ_{Li}, clock noise, ϕ_{Cij}, spacecraft motion, ϕ_{Xij}, and shot noise, ϕ_{Sij} with i and j representing the numbers of the local and distant spacecraft, respectively.

on the central spacecraft can be rewritten in the compact form:

$$\Phi_{A1} = \begin{bmatrix} \phi_{A13}(\omega) \\ \phi_{A12}(\omega) \end{bmatrix} = [\mathbf{N}_L + \mathbf{N}_S + \mathbf{N}_C + \mathbf{N}_X], \quad (61)$$

where $\mathbf{N}_L$ is the laser noise sensed at the central spacecraft photorecievers, $\mathbf{N}_S$ is the shot noise, $\mathbf{N}_C$ is the clock noise, and $\mathbf{N}_X$ is the optical bench displacement noise. These are given by

$$\mathbf{N}_L = \begin{bmatrix} P_{12}(\omega)\phi_{L1}(\omega) \\ P_{13}(\omega)\phi_{L1}(\omega) \end{bmatrix},$$

$$\mathbf{N}_S = \begin{bmatrix} \phi_{S12}(\omega) + \phi_{S21}(\omega) \\ \phi_{S13}(\omega) + \phi_{S31}(\omega) \end{bmatrix},$$

$$\mathbf{N}_C = \begin{bmatrix} \Delta_{12}(C_1(\omega) + C_2(\omega)) \\ \Delta_{13}(C_1(\omega) + C_3(\omega)) \end{bmatrix}, \quad (62)$$

$$\mathbf{N}_X = \begin{bmatrix} -\phi_{X12}(\omega)(1 + e^{-i2\omega\tau_{12}}) - 2\phi_{X21}(\omega) \\ -\phi_{X13}(\omega)(1 + e^{-i2\omega\tau_{13}}) - 2\phi_{X31}(\omega) \end{bmatrix},$$

where we have dropped the time delays in uncorrelated noise terms and assumed the heterodyne frequency on spacecraft 2 and 3 is equal to the one-way Doppler shift.

The frequency noise at the laser output with the common arm-locking control loop closed (point $O1$ in Fig. 8) is given by

$$\phi_{O1}|_+(\omega) = \phi_{L1}(\omega) - G_1(\omega)\phi_{B1}|_+(\omega),$$

$$= \frac{\phi_{L1}(\omega)}{1 + G_1(\omega)P_+(\omega)}$$

$$- \frac{G_1(\omega)}{1 + G_1(\omega)P_+(\omega)}\mathbf{S}_+[\mathbf{N}_S + \mathbf{N}_C + \mathbf{N}_X], \quad (63)$$

where $\phi_{B1}|_+ = \mathbf{S}_+\Phi_{A1}$. The control loop acts differently on laser frequency noise, compared to noise from other sources. In the high gain limit, the laser noise is suppressed by the closed loop gain, $P_+(\omega)G_1(\omega)$, whereas the other noise sources are maximumly imposed on the laser light.

The closed loop laser frequency noise for other arm-locking sensors can be calculated in a similar fashion. The vector representation and frequency response of different arm-locking sensors are listed in Table I. The closed loop noise at the laser output for the dual arm locking is given by

$$\phi_{O1}|_D(\omega) = \phi_{L1}(\omega) - G_1(\omega)\phi_{B1}|_D(\omega),$$

$$= \frac{\phi_{L1}(\omega)}{1 + G_1(\omega)P_D(\omega)}$$

$$- \frac{G_1(\omega)}{1 + G_1(\omega)P_D(\omega)}\mathbf{S}_D[\mathbf{N}_S + \mathbf{N}_C + \mathbf{N}_X], \quad (64)$$

where $\phi_{B1}|_D = \mathbf{S}_D\Phi_{A1}$.

B. The noise floor of arm locking

Armed with Eqs. (63) and (64), the noise floor of common and dual arm locking can be found. In this section we neglect laser frequency noise, equivalent to assuming the controller has infinite gain. In Sec. VIII an arm-locking controller is designed and the total noise budget, including laser noise, is plotted in Sec. IX. In the limit of high controller gain, noise sources other than laser frequency noise have little dependence on the controller gain, depending primarily on the sensor and the transfer function into the phase measurement.[5]

The noise floors of common and dual arm locking are plotted in Figs. 9 and 10 respectively, in units of frequency noise. These figures were generated assuming high controller gain, the maximum arm length difference that occurs in the mission, $2\Delta\tau = 0.51$ s, and parameters listed in Table IV. The total noise (dashed black curve) is a quadrature sum of shot noise (red curve), spacecraft motion (green curve), and the clock noise (blue curve). For the parameters used here, clock noise represents the limiting noise source of dual arm locking below 20 mHz and spacecraft motion represents a noise limit at frequencies above this. Note that clock noise is linearly dependent on the heterodyne frequency at each phase meter and this noise budget has the worst combination of heterodyne frequencies that can occur for dual arm locking: a maximum difference in Doppler shifts between the two arms, $\Delta_{13} - \Delta_{12} = 29$ MHz. In the science band, shot noise is always smaller than both the clock and the spacecraft motion, though it dominates above the band as clock noise and spacecraft motion roll off.

Also plotted in Figs. 9 and 10 is the expected TDI capability (light green curve), equal to the frequency noise requirement before TDI is applied. The amount of frequency noise suppression of TDI will be limited primarily by the time-delay errors. For the currently expected time-delay error of 3 ns [30] (equivalent of 1 m interspacecraft ranging error), TDI is capable of suppressing 300 Hz/$\sqrt{\text{Hz}}$ down to the required residual frequency noise [31] (frequency noise equivalent displacement is 2 pm/$\sqrt{\text{Hz}}$ per interspacecraft link). The TDI capability is given by

$$\tilde{\nu}_{\text{TDI}}(f) \approx 300 \times (1 + (3 \text{ mHz}/f)^2)\frac{\text{Hz}}{\sqrt{\text{Hz}}}, \qquad (65)$$

where the TDI capability is relaxed below 3 mHz, where acceleration noise of the proof mass becomes significant.[6]

Comparison of Figs. 9 and 10 shows the noise floor of common arm locking is lower than that of dual arm locking

FIG. 9 (color online). Noise of common arm locking at the laser output. The total comprises clock noise, spacecraft motion, and shot noise. This noise budget is plotted for arm length mismatch $2\Delta\tau = 0.51$ s, corresponding to the maximum arm length mismatch.

over most of the science band, although it peaks higher at frequencies corresponding to nulls in the common arm-locking sensor. The noise floors of both common and dual arm locking are substantially lower than the expected TDI capability. The noise floor in Fig. 10 is the optimal noise performance of dual arm locking, as it is plotted with the maximum arm length difference. While the noise floor of
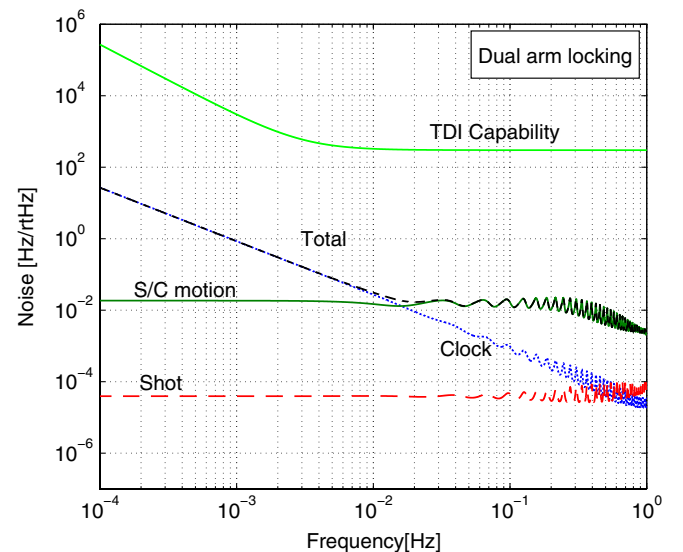
FIG. 10 (color online). Noise of dual arm locking at the laser output. The total comprises clock noise, spacecraft motion, and shot noise. This noise budget is plotted for arm length mismatch $2\Delta\tau = 0.51$ s, corresponding to the maximum arm length mismatch.

---

[5]The high controller gain assumption mentioned here is valid over the LISA science band as the magnitude of the controller gain is always greater than 100. If the controller gain is low, the noise coupling will be reduced.

[6]An alternate estimate of the TDI capability used in the FCST White Paper is $\tilde{\nu}_{\text{TDI}}(f) \approx 300 \times \sqrt{1 + (3 \text{ mHz}/f)^4}$ Hz/$\sqrt{\text{Hz}}$ [28].

TABLE IV. LISA parameters and amplitude of noise sources.

Parameter	Symbol	Value	Units
Average arm length	$\bar{L}$	5×10^9	m
Differential arm length	ΔL	$\leq 76\,500\,000$	m
Laser wavelength	λ	1064	nm
Doppler shift arm 13	Δ_{13}	15	MHz
Doppler shift arm 12	Δ_{12}	-14	MHz
Fluctuations of clock	$\tilde{y}(f)$	$2.4 \times 10^{-12}/\sqrt{f}$	$1/\sqrt{\text{Hz}}$
Shot noise	ϕ_{Sij}	10	μ cycles/$\sqrt{\text{Hz}}$
Spacecraft motion	ϕ_{Xij}	$2.5 \times \sqrt{1 + (f/0.3 \text{ Hz})^4}$	mcycles/$\sqrt{\text{Hz}}$
TDI capability	$\tilde{\nu}_{\text{TDI}}(f)$	$300 \times (1 + (3 \text{ mHz}/f)^2)$	Hz/$\sqrt{\text{Hz}}$

dual arm locking varies with inverse proportionality to the arm length mismatch, the noise floor of common arm locking is largely independent of arm length mismatch. Only the magnitude of the peaks at frequencies of $f = 1/\bar{\tau}$ and integer multiples change with differential arm length change. The dual arm-locking noise floor is plotted with smaller arm length mismatches in Fig. 11. The lower curve (dotted black curve) is plotted with $2\Delta\tau = 0.026$ s, corresponding to the minimum arm length that arm locking would have to operate with if all interspacecraft links are available and the central spacecraft were switched to give the maximum arm length difference [29]. The noise floor is a factor of 100 below the TDI capability at the closest point, showing that if all three interspacecraft links are

available, the noise floor of dual arm locking is sufficient for the entire mission.

In the case where an interspacecraft laser link fails, only two arms will be available, and therefore the central spacecraft cannot be switched when the arm length mismatch becomes small. In this case, the arm length difference will pass through zero twice per year (Fig. 34) and at this time the noise floor becomes infinite. The upper curve (dashed blue) in Fig. 11 shows the smallest arm length mismatch where the total noise floor is below the TDI capability, which occurs for $2\Delta\tau = 150$ μs, equivalent to $2\Delta L = 44$ km. Here, the clock noise, the dominant effect, becomes equal to the TDI capability near 3 mHz. The spacecraft motion is also less than a factor of 10 away from the TDI capability at this arm length mismatch. With arm length mismatches smaller than this, the TDI capability cannot be met with dual arm locking.

The variation of the dual arm-locking noise floor due to the changing arm length mismatch can be seen in Fig. 12. This shows the noise sources at 3 mHz over the first two years of the LISA mission assuming only two of the three LISA arms are available. In this case, the noise floor at 3 mHz is below the TDI capability for the vast majority of the time and breaches the TDI capability for only short periods, twice per year. It also provides some indication of how infrequently and how short a duration dual arm locking cannot meet the TDI capability in case of a critical failure of one arm. The noise performance is insufficient to meet the TDI capability for approximately 1 h, twice per year.
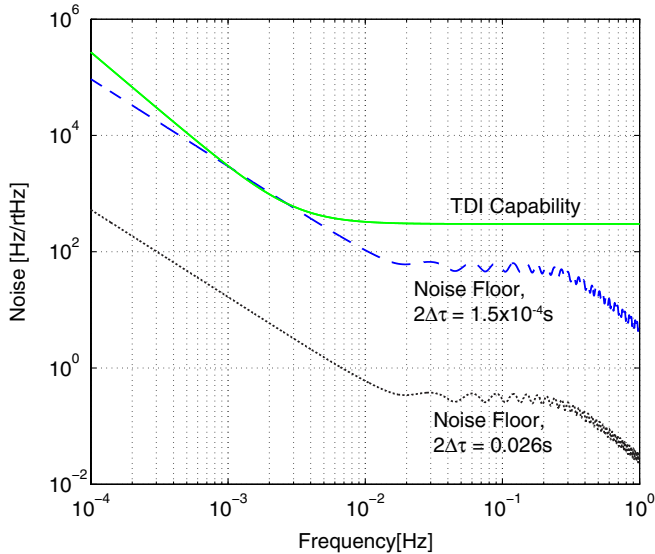
FIG. 11 (color online).   Total noise of dual arm locking at the laser output for different arm length mismatches. The lower curve has arm length mismatch of $2\Delta\tau = 0.026$ s, corresponding to the minimum arm length mismatch that occurs during the mission if any two of three arms are available to choose from. The upper curve has arm length mismatch of $2\Delta\tau = 1.5 \times 10^{-4}$ s, which is the smallest arm length mismatch that the total noise is below the TDI capability (green solid curve).

VII. MODIFICATION OF THE DUAL ARM-LOCKING SENSOR

The benefits of the dual arm-locking sensor in terms of achieving high gain across the science band as well as moving the first null in the sensor to above 2 Hz are significant, but the laser frequency pulling that occurs in steady state is unsustainable. The frequency pulling at lock acquisition is also larger than in common arm locking. In terms of noise performance, for the majority of the LISA orbit the noise floor of dual arm locking is well below the
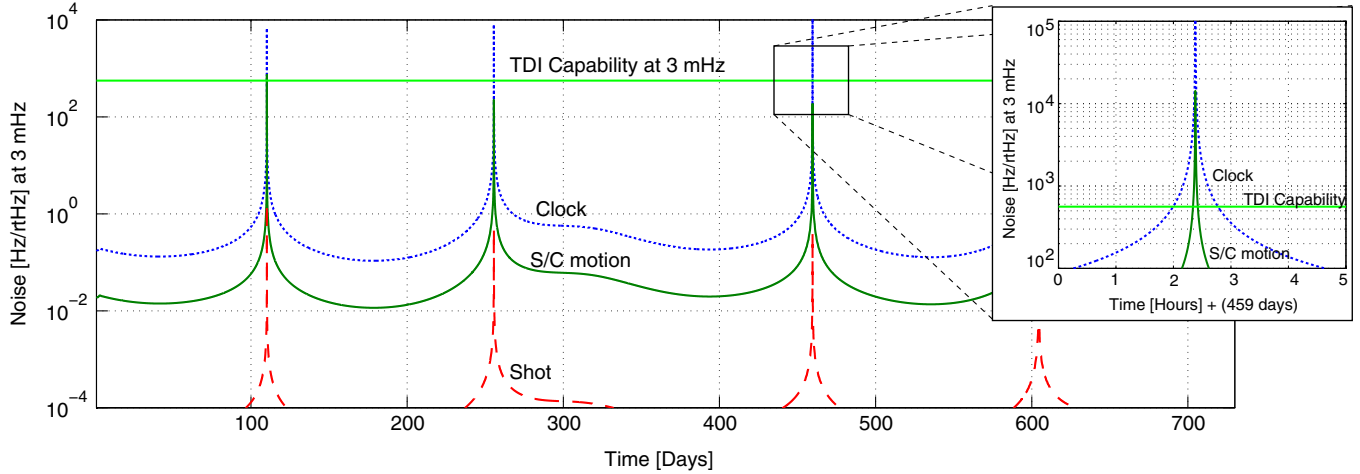
FIG. 12 (color online). The noise sources of dual arm locking measured at 3 mHz over the first two years of the LISA mission. This plot assumes only two of the three LISA arms are available, preventing the central spacecraft from being switched at small arm length mismatch. The heterodyne frequency assumed for the clock noise curve here is pessimistic, as we have assumed the worst case that occurs in the mission ($\Delta_{12} - \Delta_{13} = 29$ MHz) for the duration of this plot. The heterodyne frequency over the mission lifetime depends on the Doppler shift, whose variation we have neglected for simplicity.

TDI capability. However, when the arm length mismatch is small the noise performance of dual arm locking is degraded substantially. Here we introduce a modification to the dual arm-locking sensor to combine the benefits of common and dual arm locking.

The modified dual arm-locking sensor comprises the common arm sensor at frequencies below the first null of the arm response and the dual arm-locking sensor at frequencies above the first null, with a smooth transition between the two. This sensor provides the stability and gain advantages of dual arm locking and recovers frequency pulling characteristics and the low-frequency noise floor of common arm locking. There are no hardware changes associated with the control system modification.

A. Design of the modified dual arm-locking sensor

A block diagram of the modified dual arm-locking sensor is shown in Fig. 13. The Bode plot of the modified dual arm-locking sensor is plotted in Fig. 14 (grey curve) along with the dual arm-locking sensor proposed by Sutton and Shaddock [15] (blue curve). The sensor is located on the "central" spacecraft and uses the usual interspacecraft phase measurements from two phase meters that measure the interspacecraft signal, $\phi_{A13}(\omega)$ and $\phi_{A12}(\omega)$ (assuming spacecraft 1 is the central spacecraft). These phase measurements are combined to make the common and difference sensors, by taking the sum and difference, respectively. These combinations are then used to construct the modified dual sensor.

The modified dual arm-locking sensor is designed so that the common arm sensor dominates below the first null of the arm ($f < 1/\bar{\tau}$) and the dual sensor dominates above this frequency. The components of the modified sensor are

plotted in Fig. 15. The frequency response of the sensor is given by

$$P_M(\omega) = \underbrace{F_C(\omega)P_+(\omega)}_{\text{common part}} + \underbrace{F_D(\omega)P_D(\omega)}_{\text{dual part}}, \qquad (66)$$

where the functions $F_C(\omega)$ and $F_D(\omega)$ are filters designed to smooth the crossover from the common to dual sensors given by

$$F_C(\omega) = \frac{g_a g_b(s + z_b)}{s(s + p_b)}, \qquad (67)$$
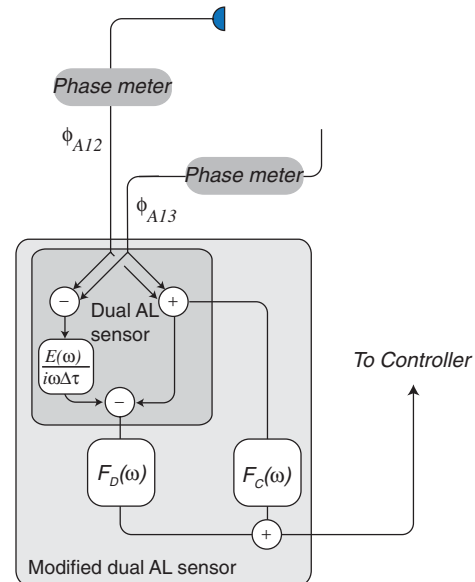
FIG. 13 (color online). Block diagram of the modified dual arm-locking sensor.
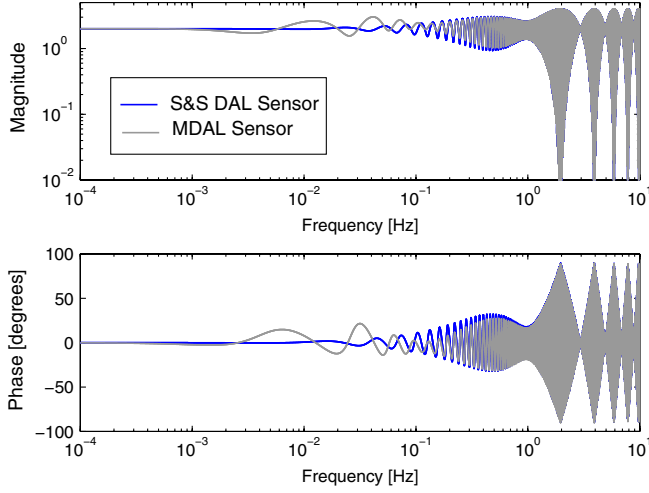
FIG. 14 (color online). Bode plot of the modified dual arm-locking sensor (grey curve) and the Sutton and Shaddock [15] (S&S) dual arm-locking sensor (blue curve).

$$F_D(\omega) = \frac{g_c g_d g_e s^4}{(s + p_c)(s + p_d)(s + p_e)^2}, \qquad (68)$$

with the parameters given in Table V.

Equation (66) can be rewritten as a function of the common and difference sensors,

$$P_M(\omega) = P_+(\omega)H_+(\omega) - P_-(\omega)H_-(\omega), \qquad (69)$$

with

$$H_+(\omega) = F_C(\omega) + F_D(\omega), \qquad (70)$$

$$H_-(\omega) = \frac{E(\omega)}{i\omega\Delta\tau}F_D(\omega). \qquad (71)$$
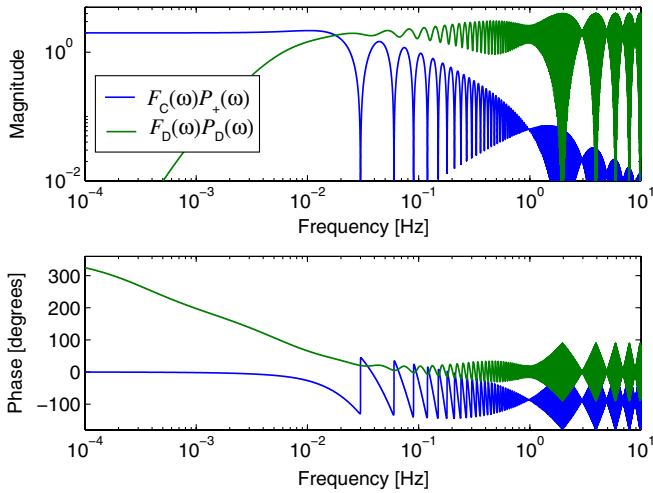
FIG. 15 (color online). Common and dual components of the modified dual arm-locking sensor. The sum of these gives the modified dual arm-locking sensor.

TABLE V. Parameters of modified dual arm-locking filters.

Filter	Zeros (rad/s)	Poles (rad/s)	Gain
$F_C(\omega)$		$p_a = 0$	$g_a = (\bar{\tau})^{-1}$
	$z_b = 2\pi \times 5/(13\bar{\tau})$	$p_b = 2\pi \times 5/(2\bar{\tau})$	$g_b = p_b/z_b$
$F_D(\omega)$	0	$p_c = 7/(5\bar{\tau})$	$g_c = 1$
	0	$p_d = 11/(20\bar{\tau})$	$g_d = 1$
	0	$p_e = 2\pi \times 1/(90\bar{\tau})$	$g_e = 1$

For the sensor in Fig. 14, $F_C(\omega)$ has a pole at DC along with a lead compensator with a zero at $5/(13\bar{\tau})$ and a pole at $5/(2\bar{\tau})$. $F_D(\omega)$ is a high pass filter made from four zeros at DC plus poles at $7/(10\pi\bar{\tau})$, $11/(20\pi\bar{\tau})$, and two poles at $1/(90\bar{\tau})$. The frequency response of the modified dual arm-locking sensor is similar to the dual arm-locking sensor, with an almost flat response below the first null with a magnitude of 2.

B. Frequency pulling in modified dual arm locking

Following the formalism set out in Sec. IV, the laser frequency pulling in modified dual arm locking is

$$\nu_{\mathrm{CL}}|_M = \frac{-G_1(\omega)\mathbf{S}_M\mathbf{V}_{\mathrm{DE}}}{1 + G_1(\omega)P_M(\omega)}, \qquad (72)$$

where $\mathbf{S}_M$ is the signal mapping vector given in Table I. As in dual arm locking, there will be pulling due to both the common and differential errors in the Doppler frequency. The frequency responses written in terms of Eqs. (70) and (71) are

$$Y_M^{(\pm)}(\omega) = \frac{\nu_{\mathrm{CL}}|_M}{\nu_{\mathrm{DE}\pm}} = \frac{-G_1(\omega)H_\pm(\omega)}{1 + G_1(\omega)P_M(\omega)}, \qquad (73)$$

where the $+$ is used for the common path and the $-$ for the difference path. Figure 16 is a block diagram showing where the Doppler error enters the modified dual arm-locking sensor.
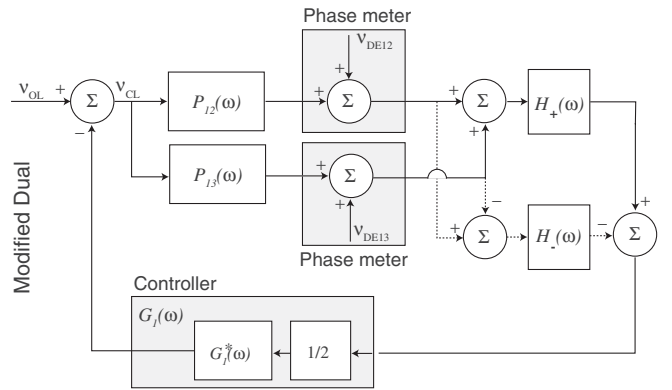
FIG. 16. Block diagram of the modified arm-locking control system showing where the Doppler frequency errors ν_{DE12} and ν_{DE13} enter the control loop.

Pulling at lock acquisition

The frequency responses at lock acquisition can be found using Eq. (73) with the appropriate $+$ or $-$ sign along with Eqs. (34) and (35). The frequency responses are written compactly as

$$\mathcal{V}_M^{(\pm)}(\omega) = \frac{-G_1(\omega)H_\pm(\omega)}{1 + G_1(\omega)P_M(\omega)}, \tag{74}$$

$$\mathcal{G}_M^{(\pm)}(\omega) = \frac{-G_1(\omega)H_\pm(\omega)}{i\omega(1 + G_1(\omega)P_M(\omega))}, \tag{75}$$

$$\mathcal{A}_M^{(\pm)}(\omega) = \frac{G_1(\omega)H_\pm(\omega)}{2\omega^2(1 + G_1(\omega)P_M(\omega))}, \tag{76}$$

again with the $\pm$ set to a $+$ for the common path and the $-$ for the difference path.

C. Noise performance

For modified dual arm locking, the noise at the laser output is given by

$$\phi_{O1}|_M(\omega) = \frac{\phi_{L1}(\omega)}{1 + P_M(\omega)G_1(\omega)}$$
$$- \frac{G_1(\omega)}{1 + P_M(\omega)G_1(\omega)}\mathbf{S}_M[\mathbf{N}_S + \mathbf{N}_C + \mathbf{N}_X]. \tag{77}$$

The improved noise performance of modified dual arm locking can be seen by comparing the total noise in Fig. 17 to the upper curve in Fig. 11. Figure 17 was plotted assuming the controller has infinite gain (so laser frequency noise is suppressed to zero). The noise floor of
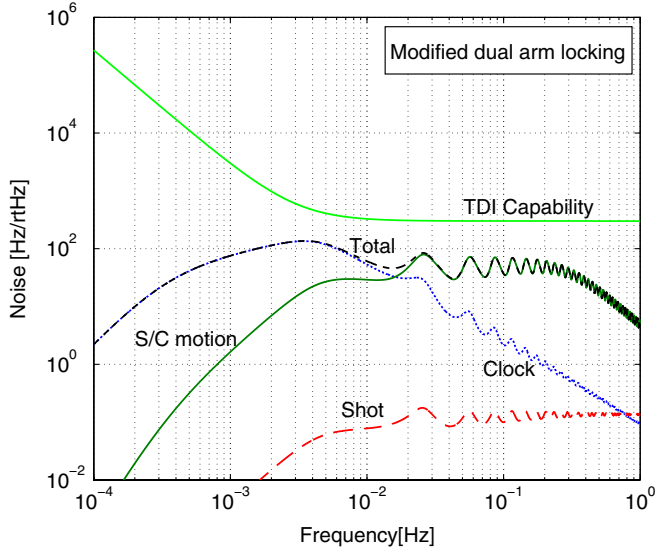
FIG. 17 (color online).   Noise at the laser output for modified dual arm locking with arm length mismatch of $2\Delta\tau = 1.5 \times 10^{-4}$ s.

modified dual arm locking is similar to that of dual arm locking above ~ 10 mHz but asymptotes to the noise floor of common arm locking below this. The noise floor of modified dual arm locking at this arm length mismatch no longer breaches the TDI capability.

VIII. DESIGN OF THE ARM-LOCKING CONTROLLER

The arm-locking controller is designed for a sensor that has a flat frequency response below 2 Hz with a magnitude of 2, and above 2 Hz has nulls in the response and a maximum amplitude of 4. Both the dual and modified dual arm-locking sensors have this frequency response. This factor of 2 is normalized out of the controller by including a $1/2$ multiplier at the beginning of the controller. Although the controller is designed for the maximum arm length mismatch, it will operate stably for smaller arm length mismatch.

A. Goal of the arm-locking control loop

The goal is to design a controller such that the arm-locking control system has sufficient gain across the LISA science band to suppress the laser noise to lower than the TDI capability. The required suppression of laser noise, $S_{\text{req}}(f)$, is a ratio of the laser noise before arm locking, $\tilde{\nu}_{\text{OL}}(f)$, and the TDI capability,

$$S_{\text{req}}(f) = \frac{\tilde{\nu}_{\text{OL}}(f)}{\tilde{\nu}_{\text{TDI}}(f)}. \tag{78}$$

If arm locking operates without any prestabilization, ν_{OL} is given by Eq. (16). If we assume this level of laser frequency noise and a time-delay error of 3 ns, the required suppression is

$$\begin{aligned} S_{\text{req}}(f) &= \frac{30/[f/\text{Hz}]\,\frac{\text{kHz}}{\sqrt{\text{Hz}}}}{300 \times (1 + (2.8\text{ mHz}/f)^2)\,\frac{\text{Hz}}{\sqrt{\text{Hz}}}}, \\ &= \frac{100/[f/\text{Hz}]}{1 + (2.8\text{ mHz}/f)^2} \end{aligned} \tag{79}$$

for $100\ \mu\text{Hz} \leq f \leq 1$ Hz.

If prestabilization is implemented the required gain will be relaxed.

B. Constraints on the controller design

Compared to a standard phase-locking control loop, the arm-locking control loop has two additional design constraints. These are
  (1) The controller should have appropriate low-frequency filtering to limit the laser frequency pulling.
  (2) The controller must allow for the nulls in the sensor and the additional phase delay associated with them.

The nulls in the dual arm-locking sensor occur at frequencies above 2 Hz.

These additional constraints limit the achievable gain in the LISA science band and necessitate careful design to ensure loop stability.

In the following sections we design a controller in two parts, treating the low-frequency design (at $f < 1$ mHz) and high-frequency design (at $f > 1$ Hz) separately. Finally, we combine the parts to complete the controller design.

C. Low-frequency filtering

In Sec. IV the laser frequency pulling that arises at lock acquisition and in steady state operation was studied. At lock acquisition, it was found that low-frequency filtering is required to limit frequency pulling due to imperfect knowledge of the Doppler frequency, Doppler rate, and second time derivative of the Doppler frequency. The frequency pulling that occurs for modified dual arm locking, calculated in Sec. VII B, is almost identical to that calculated in Sec. IV for common arm locking.

The lower bound on the lower unity-gain frequency for common arm locking [Eq. (43)] was designed to be $f_{AC} \geq 4.8 \times 10^{-6}$ Hz. If the Doppler frequency estimate has an error of $\nu_{0+} = 600$ kHz (free-running laser for an averaging time of 200 s), the pulling due to the Doppler frequency error will be under 460 MHz, 4.6% of the mode-hop-free range.[7]

The frequency pulling at lock acquisition due to error in the Doppler rate and second time derivative of the Doppler frequency can be limited by further low-frequency filtering. We find that three unity-gain high pass filters with a corner at 0.8 μHz placed in series with the rest of the controller are sufficient to limit this frequency pulling. This low-frequency part of the controller limits the frequency pulling in steady state to less than a 10 MHz peak to peak for modified dual arm locking.

D. Rolling up the gain at low frequencies

To ensure a stable control system the controller-sensor system crosses the lower unity-gain frequency, f_{AC}, with a slope of f. To optimize the gain in the LISA science band we consider various slopes that can be used to roll the gain up steeply. To design the roll up we set a >30 deg phase margin at the unity-gain frequency, and aim for the maximum gain at 100 μHz [$S_{req}(100$ μHz$) = 10^3$ is the requirement].

Accounting for the ~ 30 deg added by the 0.8 μHz high pass filters, a phase margin of 30 deg and the f slope for crossing the unity-gain frequency, leaves an additional 30 deg of phase at 4.8 μHz, which can be allocated to the increased roll up of the controller. We find that an

additional f^5 roll up with 5 zeros at 36.6 μHz and 5 poles at 185 μHz gives a gain at 100 μHz of ≈ 1900 and meets the phase requirements.

E. High-frequency design of the arm-locking controller

The nulls in the dual arm-locking sensor mean careful design of the controller is needed to ensure loop stability and to limit noise amplification. The nulls in the sensor have additional phase associated with them and mean that there are many unity-gain crossings above the first null (located at 2 Hz for maximal arm length mismatch).

To design the controller slope above 2 Hz we account for all phase delays in the control loop, specify a phase margin, then allocate the remaining phase difference from 180 deg to the slope of the controller. The delays in the control system are summarized in Table VI. A 30 deg phase margin (θ_{margin}) has been chosen at frequencies where there are nulls in the sensor ($f > 2$ Hz for the dual arm-locking sensor). The delays accounted for are the delay associated with the arm-locking sensor, θ_{sensor}, the delays in the piezo-electric transducer (PZT) actuator, τ_{act}, the phase meter processing, τ_{pm}, and in the interaction with the transponder spacecraft and the prestabilization loop, denoted as τ_{trans} and τ_{ps}, respectively.[8] The remaining phase to be allocated to the controller is

$$\theta_{controller} = 180 - \theta_{margin} - \theta_{sensor} - \theta_{delay}, \qquad (80)$$

where θ_{delay} is the total phase due to delays in the control loop given by

$$\theta_{delay} = 360 f(\tau_{act} + \tau_{pm} + \tau_{trans} + \tau_{ps}). \qquad (81)$$

F. Phase of the sensor at unity-gain points

In arm-locking studies published to date [6,15] the phase delay associated with the nulls in the sensor has been set to $\theta_{sensor} = -\pi/2$. This phase delay was allocated because it is the maximum possible phase delay of the sensor at the nulls [6]. Here, we show that this allowance is overly conservative when the controller gain is low. To determine the sensor phase at frequencies where the total open loop gain crosses unity, $\theta_{sensor}|_{UG}(\omega)$, we solve for the phase of the sensor when the loop gain has a magnitude of 1, $|G_L(\omega)| = 1$. The open-loop frequency response of the control system is

$$G_L(\omega) = \frac{G_1^*(\omega)}{2} P_M(\omega) e^{-i\theta_{delay}}. \qquad (82)$$

The common arm-locking sensor dominates the frequency response of modified dual arm-locking above the first null;

$$P_M(\omega)|_{f > (1/2\Delta\tau)} \approx P_D(\omega) \approx P_+(\omega), \qquad (83)$$

---

[7]The separation of mode hops in the Nd:YAG NPRO laser are typically ~ 10 GHz.

[8]The phase delay of the prestabilization control loop can be removed, as suggested by Sheard *et al.* [32].

TABLE VI.   Arm-locking system delays.

Type of delay	Symbol	Delay	Notes
Phase margin	θ_{margin}	30°	Control system margin
Arm-locking sensor	$\theta_{sensor}\|_{UG}$	$-\arccos(\|2G_1^*(\omega)\|^{-1})$	Phase of the sensor at unity gain
Actuator delay	τ_{act}	5 μs	PZT delay (4 μs measured)
Phase meter processing delay	τ_{pm}	2 μs	Digital-to-analog converters have an inherent 1 μs delay
Transponding S/C phase delay	τ_{trans}	5.3 μs	30 kHz unity-gain frequency assumed [a]
Prestabilization phase delay	τ_{ps}	5.3 μs	30 kHz Unity-gain frequency assumed

[a]By approximating the phase accrued in the transponding phase-locking system (and that in the prestabilization system) by a time delay we underestimate the accrued phase at 10 kHz by 0.3 deg.

$$= 2(1 - \cos(\Delta\tau\omega)e^{-i\omega\bar{\tau}}). \tag{84}$$

We are interested in the nulls in the sensor that occur when $\cos(\Delta\tau\omega) = 1$. Thus let

$$P_M(\omega)|_{f>(1/2\Delta\tau)} \approx 2(1 - e^{-i\omega\bar{\tau}}). \tag{85}$$

Define $\theta = \pi/2 - \omega\bar{\tau}/2$, giving

$$P_M(\omega)|_{f>(1/2\Delta\tau)} = 2(1 + e^{2i\theta}). \tag{86}$$

Using the identity $1 + e^{2i\theta} = 2\cos\theta e^{i\theta}$ we see that θ is the phase of the sensor. At unity gain, $|G_L(\omega)| = |G_1^*(\omega)| \cdot 2\cos\theta_{sensor}|_{UG} = 1$. That gives $\cos\theta_{sensor}|_{UG} = 1/|2G_1^*(\omega)|$, or for the sensor phase at unity gain

$$\theta_{sensor}|_{UG} = -\arccos(|2G_1^*(\omega)|^{-1}) \quad \text{for } |2G_1^*(\omega)| \geq 1. \tag{87}$$

We have selected the negative solution for $\theta_{sensor}|_{UG}$ because that gives maximum phase delay, which is of interest for stability considerations.

At high controller gain, say $|2G_1^*(\omega)| > 100$, the point on the sensor which crosses unity gain is very close to the null. Accordingly, the phase delay of the sensor at the unity gain is $\theta_{sensor} \approx -\pi/2$. For a controller gain of $|2G_1^*(\omega)| = 1$ the peak of the sensor response will cross unity gain. The corresponding phase at this point approaches zero ($\theta_{sensor} \rightarrow 0$). The sensor phase at several unity-gain frequencies is illustrated in the Nyquist plot in Fig. 18.

With the phase associated with the sensor at unity gain and the other delays in Table VI we find that approximately 60 deg of phase can be assigned to the controller, corresponding to a controller slope of $f^{-0.66}$. With this slope, a unity-gain frequency of up to 14.9 kHz can be achieved. A Bode plot of such a controller is shown in Fig. 19. The magnitude is given by $|567/(if/\text{Hz})^{0.66}|$. The total phase of the control system (black curve) is a sum of the system delays (dotted green curve), the phase of the sensor at unity gain (dashed red curve), and phase associated with the controller (blue solid curve). Note the behavior of the system delays and the sensor phase at unity gain is complementary at high frequencies. This effect allows the control bandwidth to be increased and the controller slope

to be steeper, giving a factor of 10 higher gain at 1 Hz than without this effect. With $\theta_{sensor} = -\pi/2$ allocated, the maximal constant controller slope is $f^{-0.58}$ and the control bandwidth is 1.2 kHz, giving a gain at 1 Hz of 61.

G. The complete frequency response of the controller

The low- and high-frequency components of the controller can be combined to obtain the complete frequency response. Analytically, the controller can be designed with a precise slope at all frequencies. Here, we present a controller using only poles and zeros. A block diagram of the controller architecture is shown in Fig. 20. The controller consists of five stages. Stage 1 is the very low-
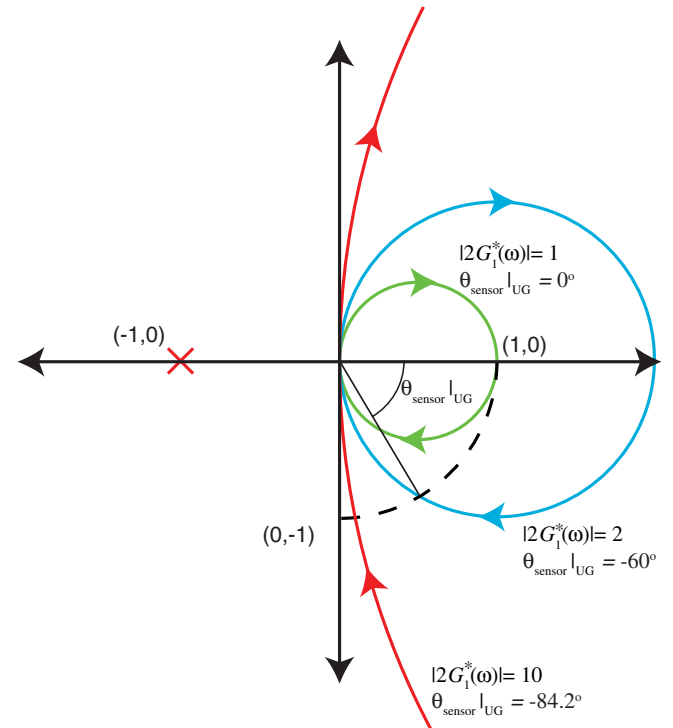

FIG. 18 (color online).   Nyquist plot of the open loop frequency response, $G_L(\omega)$, for three different controller gains, $|G_1^*(\omega)|$. The phase delay associated with the sensor corresponds to the angle from the x axis to the point at which the sensor times gain crosses the dashed line which has a radius of 1.
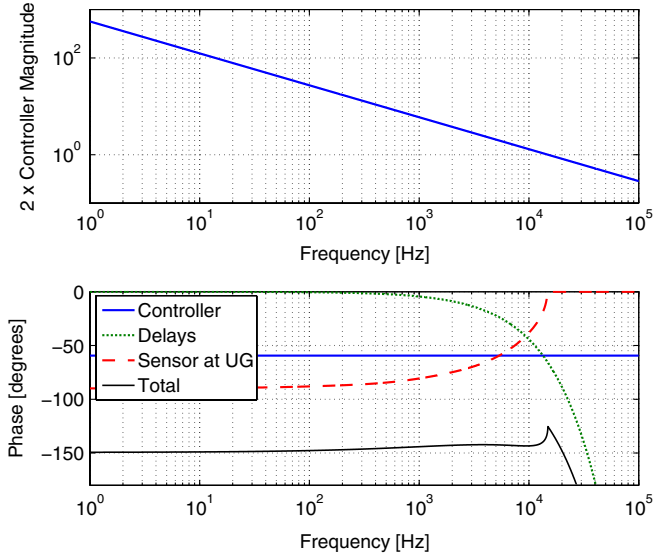
FIG. 19 (color online).   Bode plot of the arm-locking controller. The lower plot shows the total open loop phase of the control system and the three components of which it is comprised. These are the controller (− 59.4 deg), the system delays (for parameters used in Table VI), and the sensor phase at unity gain, given by Eq. (87).

frequency part of the controller and comprises three zero-pole pairs to form unity-gain high pass filters at 0.8 μHz in series. Stage 2 sets the lower unity-gain frequency and has a zero at DC and a pole at 210 μHz. Stage 3 is a lead stage, which has five zero-pole stages in series to roll up the gain steeply between the lower unity-gain frequency and the low-frequency part of the controller. Stage 4 consists of two poles in series and provides the transition between the low-frequency gain and the shallow slope high-frequency
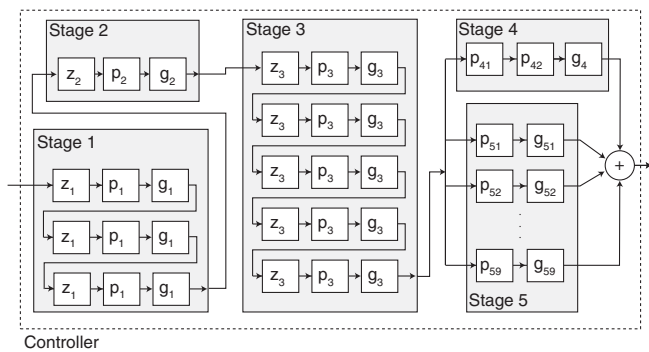
FIG. 20.   Block diagram of the arm-locking controller. The controller is built from five stages: stage 1 consists of three very low-frequency high pass filters; stage 2 defines the lower unity-gain frequency; stage 3 rolls up the gain below the LISA science band; stage 4 has two poles in parallel to effectively transition between stages 3 and 5; and stage 5 has 9 poles in parallel, with gains individually chosen to generate a slope of approximately $f^{-0.66}$.

part of the controller. Stage 5 is the shallow sloped part of the controller. It consists of nine poles in parallel, with the gain for each pole chosen to achieve the required slope of approximately $f^{-0.66}$. The frequency response of the controller is given by

$$G_1^*(\omega) = \left(\frac{g_1 s}{s + p_1}\right)^3 \times \left(\frac{g_2 s}{s + p_2}\right) \times \left(\frac{g_3(s + z_3)}{s + p_3}\right)^5$$
$$\times \left(\frac{g_4}{(s + p_{41})(s + p_{42})} + \sum_{k=1}^{9} \frac{g_{5k}}{s + p_{5k}}\right), \quad (88)$$

with values of the zeros, poles, and gains listed in Table VII.[9]

The open loop gain of the control system with the modified dual arm-locking sensor is given by

$$G_L(\omega) = G_1(\omega) P_M(\omega) e^{-i\omega(\tau_{\text{act}} + \tau_{\text{pm}} + \tau_{\text{trans}} + \tau_{\text{ps}})}. \quad (89)$$

The Bode plot of $G_L(\omega)$ is plotted in Fig. 21. Note that in this plot we have assumed no prestabilization and thus set $\tau_{\text{ps}} = 0$. It can be seen that $G_L(\omega)$ exceeds the required gain, $S_{\text{req}}(f)$, Eq. (79). Note that looking at the open loop phase is somewhat deceptive. At high frequencies it appears that the open loop phase crosses 180 deg before 1 kHz, making the 14.9 kHz bandwidth control loop unstable. In fact, the total phase at the unity-gain points is always greater than −150 deg which is indicated by the red solid curve, given by

$$\theta_{\text{UG}} = \angle G_1^*(\omega) \times \frac{180}{\pi} + \theta_{\text{sensor}}|_{\text{UG}}$$
$$+ 360 f(\tau_{\text{act}} + \tau_{\text{pm}} + \tau_{\text{trans}}), \quad (90)$$

valid for $f \geq 1/(2\Delta\tau)$.

H. Closed loop performance of the controller

The closed loop disturbance suppression function is shown in Fig. 22. This function is given by

$$S_D(\omega) = \frac{1}{1 + G_L(\omega)}. \quad (91)$$

This shows the suppression of the control loop, as well as amplification of the noise at the nulls in the sensor and above the control loop unity-gain frequency. Also plotted is the required suppression to meet the TDI capability. Note that the amplification at the nulls is always less than a factor of 2 except near the final unity-gain frequency, near 15 kHz, where the amplitude increases to 5.

---

[9]An additional low pass filter in series with the controller is generally required to roll off the loop gain at the resonance frequency of the laser PZT actuator (near 100 kHz)

TABLE VII.   Parameters of the arm-locking controller.

Stage	Zeros (rad/s)	Poles (rad/s)	Gain
1	$z_1 = 0$	$p_1 = 2\pi \times 8 \times 10^{-7}$	$g_1 = 1$
2	$z_2 = 0$	$p_2 = 2\pi \times 210 \times 10^{-6}$	$g_2 = 0.95/f_{ac} \times 1$ Hz
3	$z_3 = 2\pi \times 36.6 \times 10^{-6}$	$p_3 = 2\pi \times 185 \times 10^{-6}$ [a]	$g_3 = p_3/z_3$
4		$p_{41} = 2\pi \times 3 \times 10^{-3}$	
		$p_{42} = 2\pi \times 238 \times 10^{-3}$	$g_4 = p_{41}p_{42}$
5		$p_{51} = 2\pi \times 3 \times 10^{-3}$	$g_{51} = 1.3 \times 10^{-3} \times 1$ Hz
		$p_{52} = 2\pi \times 3 \times 10^{-2}$	$g_{52} = 3.7 \times 10^{-3} \times 1$ Hz
		$p_{53} = 2\pi \times 3 \times 10^{-1}$	$g_{53} = 4.2 \times 10^{-3} \times 1$ Hz
		$p_{54} = 2\pi \times 3$	$g_{54} = 16 \times 10^{-3} \times 1$ Hz
		$p_{55} = 2\pi \times 3 \times 10^{1}$	$g_{55} = 30 \times 10^{-3} \times 1$ Hz
		$p_{56} = 2\pi \times 3 \times 10^{2}$	$g_{56} = 69 \times 10^{-3} \times 1$ Hz
		$p_{57} = 2\pi \times 3 \times 10^{3}$	$g_{57} = 0.11 \times 1$ Hz
		$p_{58} = 2\pi \times 3 \times 10^{4}$	$g_{58} = 0.33 \times 1$ Hz
		$p_{59} = 2\pi \times 3 \times 10^{5}$	$g_{59} = 0.70 \times 1$ Hz

[a]If arm locking is implemented with prestabilization, $p_3 = 2\pi \times 178 \times 10^{-6}$.

IX. EXPECTED PERFORMANCE OF ARM LOCKING

The performance of arm locking can be predicted using the frequency pulling analysis of Sec. IV, the noise analysis of Sec. VI, the controller design given in Sec. VIII, and an assumption of the laser frequency noise. Here, we calculate noise budgets for three different initial laser noise levels: free-running laser noise, and laser noise predicted for two types of prestabilization, Fabry-Perot cavity stabilization and Mach-Zehnder stabilization.

A. Performance assuming free-running laser noise

The expected frequency pulling that would occur at lock acquisition is shown in the upper plot in Fig. 23. In this case the Doppler frequency errors are the values of ν_{0+}, γ_{0+}, and α_{0+} given in the free-running laser column in Table III. These results are near identical to those for common arm locking shown in Sec. IV because the common arm-locking sensor dominates the frequency response at low frequencies. Likewise, the result for pulling in steady state of modified dual arm locking, shown in Fig. 24, is similar

FIG. 21 (color online).   Open loop frequency response, $G_L(\omega)$, of modified dual arm locking. Also shown in the magnitude plot is the gain required to meet the TDI capability, assuming no prestabilization. In the phase plot, the red curve indicates the total phase of the control loop at unity gain [given by Eq. (90)]. The arm length mismatch is assumed to be $2\Delta\tau = 0.51$ s.
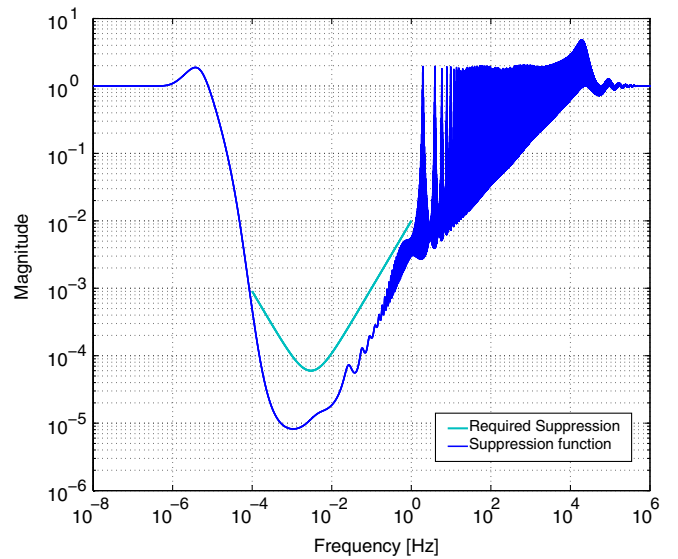

FIG. 22 (color online).   Plot of the disturbance sensitivity $S_D(\omega)$ and the required suppression $1/S_{req}(\omega)$. Plotted with $2\Delta\tau = 0.55$ s.
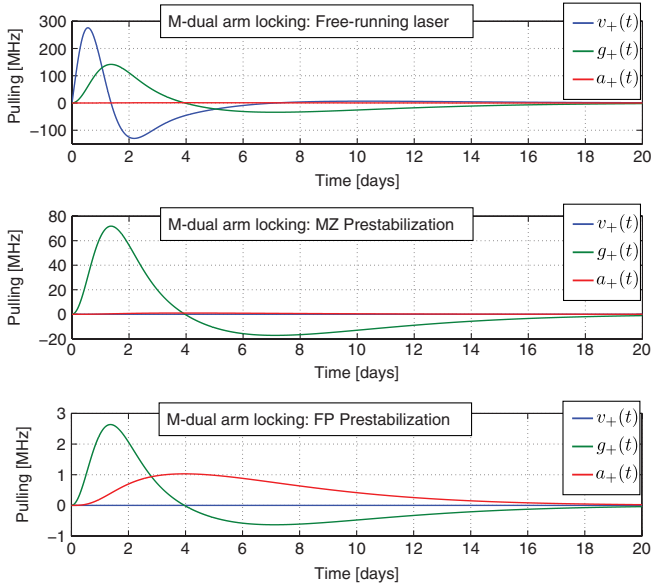
FIG. 23 (color online). The step responses of different drivers of Doppler frequency error for modified dual arm locking. The upper, middle, and lower plots assume free-running laser noise, Mach-Zehnder–type prestabilization, and Fabry-Perot cavity prestabilzation, respectively, with the Doppler frequency estimates averaged for 200 s.

to that of common arm locking, with less than 8 MHz peak-to-peak pulling. This is significantly less pulling than occurs with dual arm locking (compare the lower plot of Fig. 7 to Fig. 24), which has unsustainable pulling when the arm length mismatch is small.

Figure 25 shows the noise budget of modified dual arm locking with free-running laser noise and an arm length mismatch of $2\Delta\tau = 0.51$ s. For this arm length mismatch the laser frequency noise is the limiting noise source (the system is gain limited) with the other system noise sources well below the laser frequency noise. Figure 25 shows that even without any form of laser prestabilization, arm locking will meet the TDI capability across the entire LISA science band. At the most sensitive frequency of LISA, 3 mHz, the frequency noise is more than a factor of 4 below
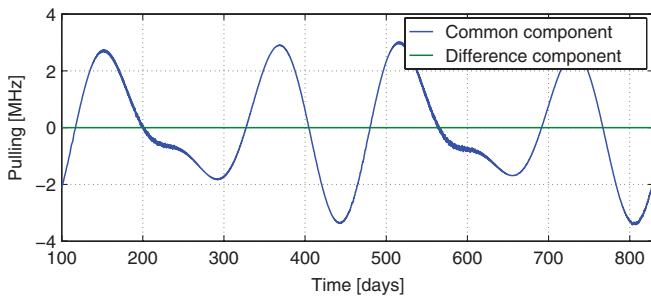
FIG. 24 (color online). The steady state laser frequency pulling of modified dual arm locking. The pulling due to the common Doppler shift is the dominant term.
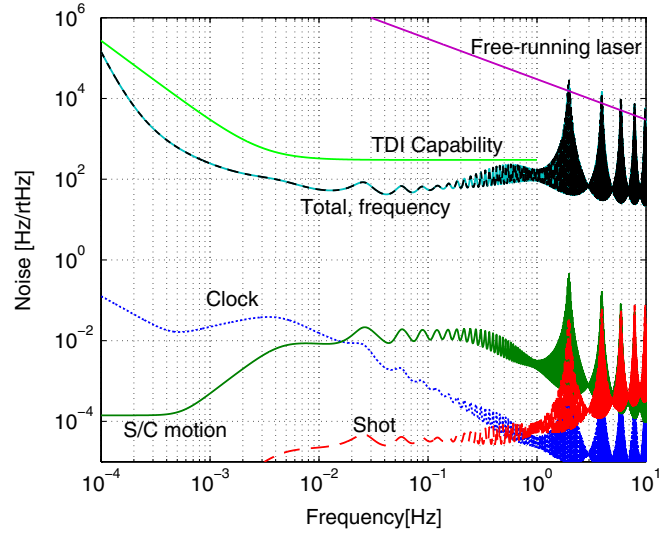
FIG. 25 (color online). The noise budget of modified dual arm locking with arm length mismatch of $\Delta\tau = 0.51$ s. The performance was calculated with free-running laser noise as an initial condition.

the TDI capability. If there is not a failure of one interspacecraft laser link, the dual arm-locking central spacecraft can be switched when the arm length mismatch becomes small, and arm locking alone has sufficient performance to meet the TDI capability for the mission.

The performance of arm locking with an interspacecraft laser link failure is similar to the no failure case. For the majority of the mission the system will be gain limited as it is in the no link failure scenario. The difference is for a few hours per year the system will become noise limited, when the arm length mismatch is close to zero. The noise performance will be insufficient to meet the TDI capability for approximately 30 min, twice per year. Note that this noise limited time could be reduced by either flying a clock with better stability or by implementing the clock noise removal algorithm inside the arm-locking sensor.[10]

B. Performance assuming prestabilized laser noise

The frequency pulling that would occur at lock acquisition assuming Mach-Zehnder and Fabry-Perot prestabilization is shown in the middle and lower plots in Fig. 23, respectively. The Doppler frequency errors assumed for ν_{0+}, γ_{0+}, and α_{0+} for the former prestabilization are given in the Mach-Zehnder column in Table III and for the latter are $\nu_{0+} = 1.68$ Hz, and $\gamma_{0+} = 0.08$ Hz/s. This shows less than 90 MHz peak-to-peak pulling over a period of 10 days for the Mach-Zehnder prestabilization or less than 4 MHz for Fabry-Perot prestabilization.

---

[10]However, to remove clock noise using this method, the clocks at the end spacecraft would need to be phase locked to the central spacecraft clock in an analogous way to the lasers.
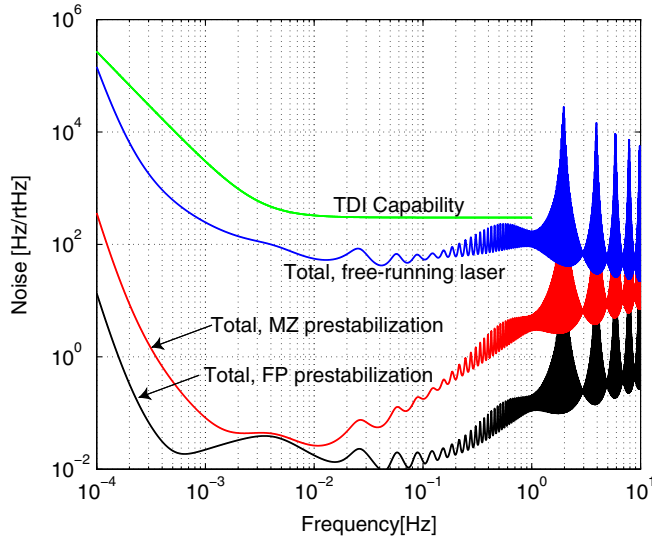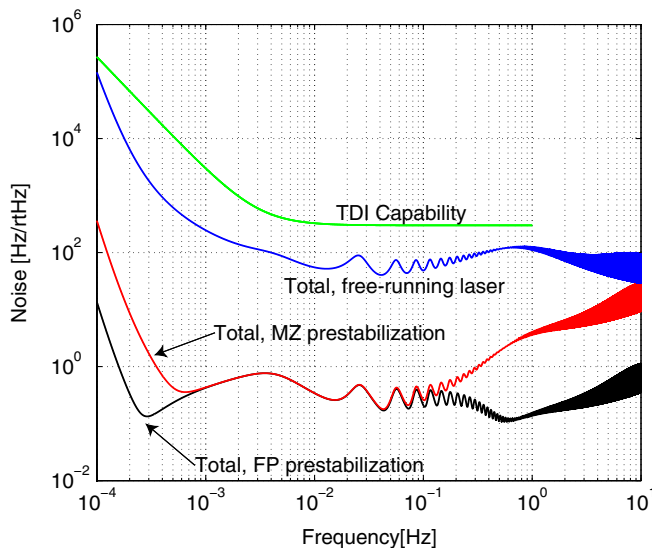
FIG. 26 (color online).   Noise floor of modified dual arm locking with different initial laser frequency noise conditions: free-running laser noise (blue curve), Mach-Zehnder prestabilization (red curve), and Fabry-Perot cavity prestabilization (black curve). Arm length mismatch of $\Delta\tau = 0.51$ s.

In Figs. 26 and 27 the total noise after arm locking is plotted for no prestabilization, Fabry-Perot cavity prestabilization, and Mach-Zehnder prestabilization. Figure 26 is plotted for the maximum arm length mismatch, while Fig. 27 is plotted for the minimum arm length mismatch, which will be used if there is no failed interspacecraft laser links. It is clear that either prestabilization type in combi-

FIG. 27 (color online).   Noise floor of modified dual arm locking with different initial laser frequency noise conditions: free-running laser noise (blue curve), Mach-Zehnder prestabilization (red curve), and Fabry-Perot cavity prestabilization (black curve). Arm length mismatch of $\Delta\tau = 0.026$ s.

nation with arm locking will deliver performance several orders of magnitude better than the TDI capability. With either prestabilization system the performance is limited by clock noise and spacecraft motion in the region of a few mHz. This is the case even with the largest arm length mismatch.

Again, the performance of arm locking with a single link failure is similar to the no failure case with prestabilization, except at some frequencies the system will be noise limited for the whole mission. The ultimate performance at 3 mHz, for example, will be entirely dictated by the noise sources. The noise floor will exceed the TDI capability as the arm length mismatch passes through zero. The performance is insufficient to meet the TDI capability for about 30 min, twice per year.

X. CONCLUSIONS

We have performed a detailed analysis of the expected performance of arm locking in LISA. This analysis includes many of the orbital effects expected on LISA: changing arm lengths and Doppler frequencies as well as laser frequency pulling due to errors in the Doppler frequency estimate. It was found that laser frequency pulling could be limited to an acceptable level by high pass filtering the control loop. We also noted that not only will the Doppler frequency error cause laser frequency pulling at lock acquisition, but because the Doppler frequencies continuously change, the error in Doppler rate can too be significant. In terms of the magnitude of the pulling, if arm locking is used without prestabilization, the Doppler frequency can be estimated to 600 kHz over 200 s, giving 460 MHz of pulling at lock acquisition for the controller designed here. This magnitude of pulling would occur only the first time the control loop is engaged, as after LISA has been operating over longer periods the Doppler frequency estimate would be improved. Less pulling at lock acquisition will be achieved if either a longer estimate of the Doppler frequency was made, or if arm locking was used in combination with prestabilization.

The noise analysis presented here included the expected dominant noise sources in arm locking: clock noise, spacecraft motion, and shot noise. It was found that clock noise and spacecraft motion are the dominant noise sources in the LISA science band and that they will limit the noise performance when the arm length mismatch is small.

We introduced a new sensor design for the dual arm-locking sensor, which uses a combination of the common and dual arm sensor at frequencies below $1/\bar{\tau}$ and the dual arm-locking sensor frequencies above $1/\bar{\tau}$. This modified dual sensor has the control system advantages of dual arm locking with the frequency pulling characteristics and low-frequency noise performance of common arm locking. Obtaining the frequency pulling characteristics of common arm locking is of particular importance, as the frequency pulling that occurs in steady state is negligible. In com-

parison, when the arm length mismatch becomes small, the pulling of dual arm locking in steady state would be large enough to drive the lasers into their mode-hop regions, compromising instrument sensitivity.

We designed an arm-locking controller which maximizes gain in the science band, minimizes frequency pulling, and has a phase margin of greater than 30 deg to ensure stability. We noted an effect where the arm-locking sensor phase changes beneficially near the unity-gain frequencies of the control system. With this effect taken into account, it was found that the control bandwidth could be up to 14.9 kHz and still maintain a 30 deg phase margin. This control bandwidth is 10 times higher than if this frequency dependent phase effect is not taken into account.

Using the noise analysis of Sec. VI and the controller design given in Sec. VIII, we calculated noise budgets for different initial laser frequency noise levels. The laser frequency noise levels we chose correspond to the noise of lasers free running, prestabilization to a Mach-Zehnder interferometer and to a Fabry-Perot cavity. A key result is that arm locking alone can meet the TDI capability. With prestabilization, the TDI capability would be met by more than 2 orders of magnitude across the science band.

We analyzed the expected performance of arm locking with and without the failure of an interspacecraft laser link. If there is no failure, arm locking will have sufficient noise performance to meet the TDI capability for the entire mission, independent of whether prestabilization is used or not (though the performance is significantly better with prestabilization). If there is a loss of one interspacecraft laser link, the noise floor of arm locking will exceed the TDI capability for approximately 30 min, twice per year, when the arm length mismatch is less than 12 km. This would occur with or without prestabilization.

ACKNOWLEDGMENTS

APPENDIX A: DOPPLER FREQUENCY ESTIMATION

The measurement concept for initial estimation of the Doppler rate of a given arm is illustrated in Fig. 28.

The transponded, interfered, and detected LISA science signal ϕ_M (M for measured) contains the Doppler signal $\nu_M = v/\lambda$, where v is the relative velocity between space-
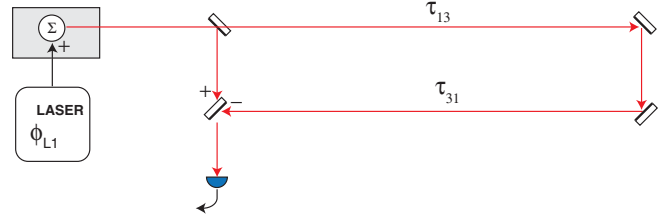

FIG. 28 (color online). Measurement of Doppler frequency before initialization of arm locking can be made by comparing the prompt and delayed (and Doppler frequency shifted) laser frequencies.

craft. The variance of the measured frequency, σ^2, is defined as the integral of the power spectral density $\tilde{\nu}_M^2(f)$:

$$\sigma^2 = \int_0^\infty df\, \tilde{\nu}_M^2(f). \tag{A1}$$

Averaging over a window of duration T introduces the filter $H(f) = \mathrm{sinc}(fT) = \sin(\pi fT)/(\pi fT)$. The phase measurement is

$$\phi_M(t) = \phi(t) - \phi(t - \tau), \tag{A2}$$

where $\phi(t)$ is the inherent phase of the laser output and τ is the round-trip travel time. Differentiating, the corresponding frequency values are

$$\nu_M(t) = \nu(t) - \nu(t - \tau). \tag{A3}$$

Equation (A1) then becomes

$$\sigma^2 = \int_0^\infty df\, \tilde{\nu}^2(f)|H(f)|^2|L(f)|^2, \tag{A4}$$

with

$$L(f) = 1 - \exp(2\pi i f\tau). \tag{A5}$$

Using

$$|L(f)|^2 = 2[1 - \cos(2\pi f\tau)] = 4\sin^2(\pi f\tau), \tag{A6}$$

$$\sigma^2 = 4\int_0^\infty df\, \tilde{\nu}^2 \mathrm{sinc}^2(fT)\sin^2(\pi f\tau). \tag{A7}$$

We consider $\tilde{\nu}(f) = f^k$, $k = [-1, -\frac{1}{2}, 0]$, corresponding, respectively, to random-walk frequency noise, flicker frequency noise, and white frequency noise. These shapes are typical for the respective sources: free-running lasers, USO phase noise, and unequal-arm Michelson interferometry limited by white phase meter noise. Analytic expressions for σ are in Table VIII, and representative numerical values of $\tilde{\nu}(f)$ and the resulting values of σ are plotted in Figs. 30 and 29, respectively.

TABLE VIII. Error in Doppler frequency estimation, σ, for various spectra of frequency noise $\tilde{\nu}(f)$. Round-trip travel time $= \tau$, averaging time $= T$, and $n = T/\tau$. Note the distinction between absolute-value brackets $|\cdots|$ and grouping brackets $[\cdots]$ or $(\cdots)$.

$\tilde{\nu}(f)$	σ
$K_F f^{-1}$	$K_F(\pi/n)\sqrt{\tau/3}\sqrt{|n-1|^3 + (n+1)^3 - 2(n^3+1)}$
$K_U f^{-1/2}$	$K_U\sqrt{\log[|1-n^{-2}||1-n^2|^{1/n^2}([n+1]/|n-1|)^{2/n}]}$
K_W	$K_W/(\sqrt{2\tau}n)\sqrt{1+n-|1-n|}$

The estimation based on USO noise is a new concept that requires some explanation. The USO signals are imposed as ≈ 10 GHz modulation sidebands on the carrier, for clock correction. Just as the carrier is transponded by phase locking the distant laser to the incoming laser, so too the USO sideband can be transponded by feeding back the sideband/sideband beat to the phase-locking input of the USO. Then at the master (local) spacecraft, the measured sideband/sideband beat is representative of the Doppler shift. The measurement is made insensitive to laser frequency noise by subtracting the measured carrier/carrier phase, leaving noise only from the clock. In this manner, the USO can substitute for an optical frequency reference for the purpose of measuring Doppler frequency.

The error in the average of the kth time derivative of the Doppler shift is a generalization of Eq. (A1):

$$\sigma_k^2 = \int_0^\infty df(2\pi f)^{2k}\tilde{\nu}_M^2(f). \tag{A8}$$

Generalizing Eq. (A7) to allow for j stages of averaging of the kth time derivative,

$$\sigma_{jk}^2 = 4\int_0^\infty df(2\pi f)^{2k}\tilde{\nu}^2\text{sinc}^{2j}(fT)\sin^2(\pi f\tau). \tag{A9}$$

For $\tilde{\nu} = f^p$, Eq. (A9) gives finite σ_{jk} only for $j \geq 1 + p + $

FIG. 30 (color online). Various assumptions of frequency noise $\tilde{\nu}(f)$ as input to estimation of the initial Doppler rate ν The uppermost curve F represents the noise in a free-running laser, $\tilde{\nu}(f) = k_f/f$, $k_f = 1 \times 10^4$ Hz$^{3/2}$; the flat W curve represents white laser frequency noise, $\tilde{\nu}(f) = K_w = 1 \times 10^4$ Hz$^{1/2}$, and the U curve is a typical USO spectrum, $\tilde{\nu}_U(f) = k\nu_0/\sqrt{f}$, where $k = 2.4 \times 10^{-12}$ and ν_0 is the laser frequency, 2.8×10^{14} Hz.

k. Therefore, to estimate the first and second derivatives of the Doppler shift ($k = 1, 2$, respectively) with white frequency noise ($p = 0$) requires at least two and three stages of averaging ($j = 2, 3$), respectively. Note that j stages of averaging requires data of duration jT. For the spectrum of free-running lasers ($p = -1$), the minimum number of averages to compute the first and second derivatives are $j = 1, 2$, respectively. We have computed σ_{jk} for $k = (0, 1, 2)$ and $p = (0, 1)$ with up to $j = 3$ stages of averaging, using the Symbolic Math package of MATLAB [33]. Sample numeric results are shown in Fig. 31.
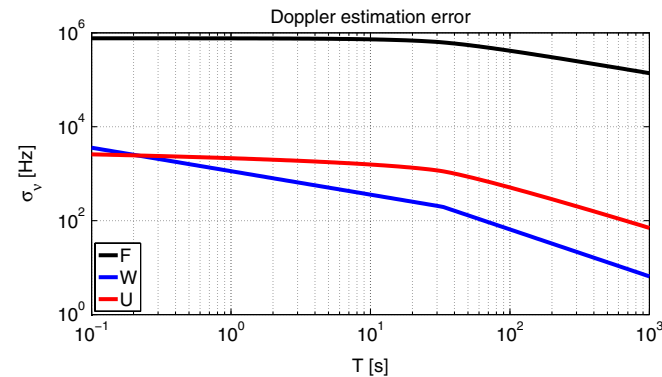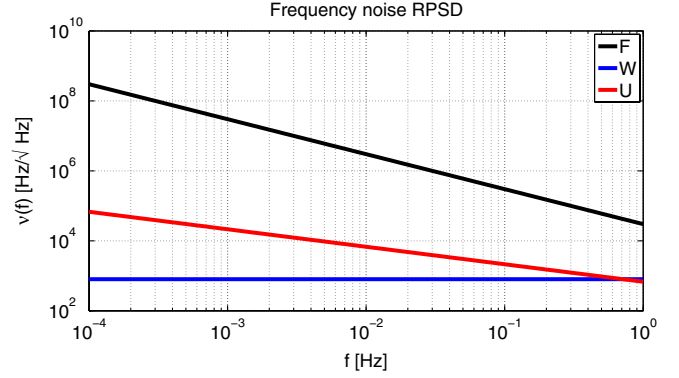

FIG. 29 (color online). Doppler estimation error $\sigma(T)$ from averaging the spectra $\tilde{\nu}(f)$ of Fig. 30 over period T.
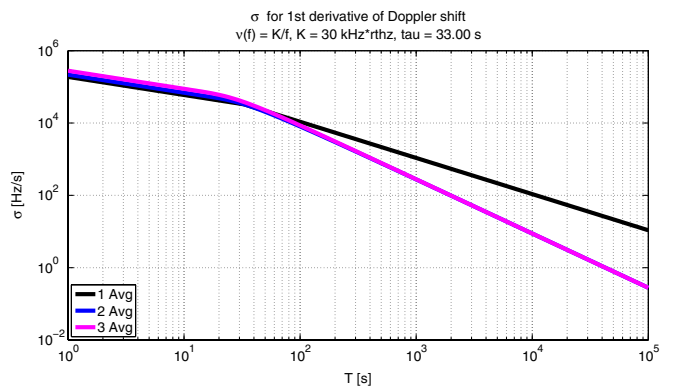

FIG. 31 (color online). Error in the estimate of the first time derivative of the single-arm Doppler shift, assuming the noise of free-running lasers, Fig. 30. For averaging times $T < \tau = 33$ s, there is no advantage to more than one stage of averaging. For $T > 33$ s, two stages of averaging gives less error than one, but there is no advantage to three stages. The estimation error from two stages, each of duration $T = 100$ s, is 8 kHz/s.
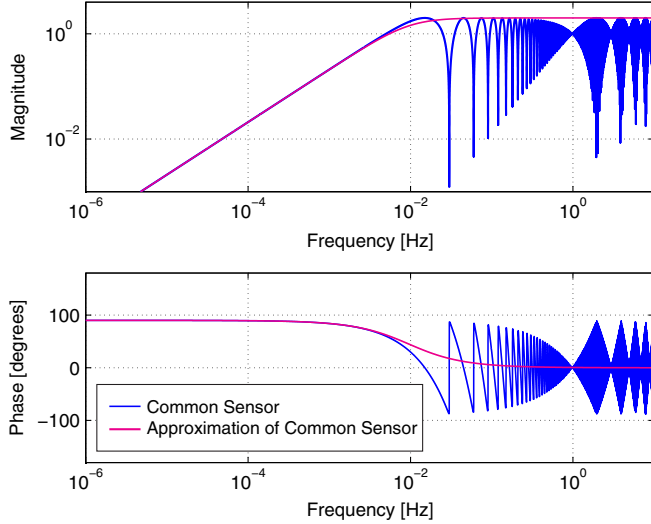
FIG. 32 (color online). Common arm-locking sensor and its approximation used in step responses.

APPENDIX B: APPROXIMATION OF THE SENSORS

In Sec. IV we performed a study of the frequency pulling caused by the closed arm-locking control loop. Because of the high computational time required to simulate the frequency pulling using the sensors in their exact form, the simulations spanning over a period of days after lock acquisition were performed using approximations of the sensors. These approximations are very good below the null frequencies, that is, for $f < 10$ mHz in common arm locking, and $f < 2$ Hz for dual arm locking. This frequency band is responsible for the most significant pulling occurs.
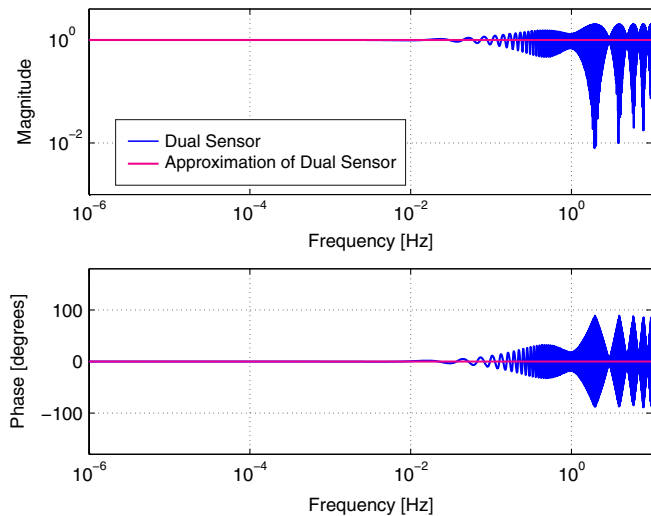
In the study of pulling in common arm locking we approximate the frequency response of the sensor by

$$P_+(\omega)|_{\text{approx}} = \frac{4s}{s + 2/\bar{\tau}}, \qquad \text{(B1)}$$

which is plotted in Fig. 32 along with the common arm-locking sensor.

In the study of pulling in dual arm locking and modified dual arm locking we approximate the frequency response of the sensor by

$$P_D(\omega)|_{\text{approx}} = 2, \qquad \text{(B2)}$$

which is plotted in Fig. 33 along with the dual arm-locking sensor.

The controllers used in calculating the frequency pulling in Sec. IV were based on the controller design presented in Sec. VIII. The shape of the common arm-locking sensor differs significantly from that of the dual arm-locking sensor (for which the controller was designed). To calculate the frequency pulling in common arm locking the controller response was modified to account for this. The controller used in common arm-locking frequency pulling calculations was simply

$$G_1(\omega) = \frac{G_1^*(\omega)}{P_+(\omega)|_{\text{approx}}}, \qquad \text{(B3)}$$

where $G_1(\omega)^*$ is given by Eq. (88).

APPENDIX C: ORBITS

The orbit data used in this paper were provided by Gath [34]. Plots of the relevant parameters are shown in Figs. 34–36.

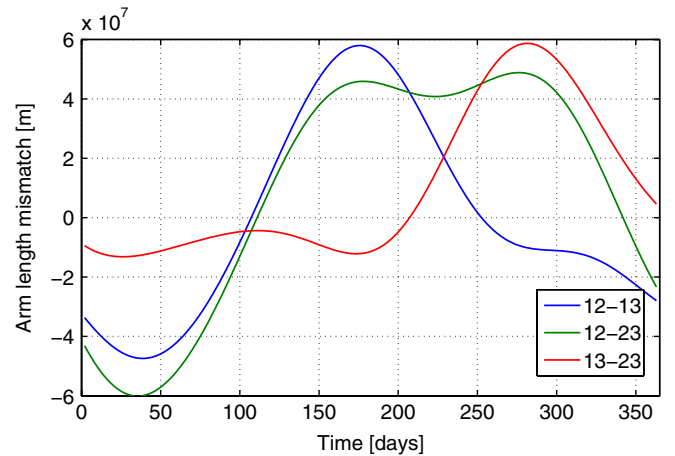FIG. 33 (color online). Dual arm-locking sensor and approximation used in step responses.

FIG. 34 (color online). Arm length mismatch of the sets of two arms. Calculations in this paper were performed using arm 12-13.
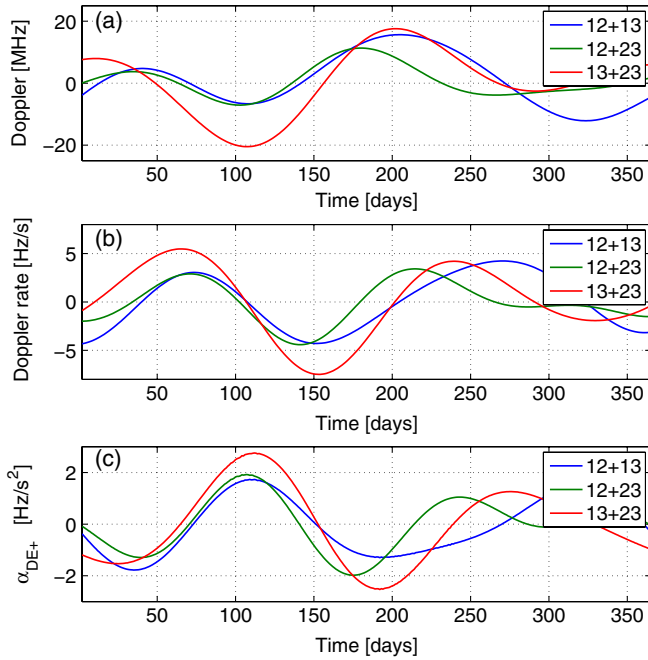
FIG. 35 (color online). (a) Common Doppler frequency, (b) common Doppler rate, and (c) 2nd time derivative of common Doppler frequency for the different arm pairs.
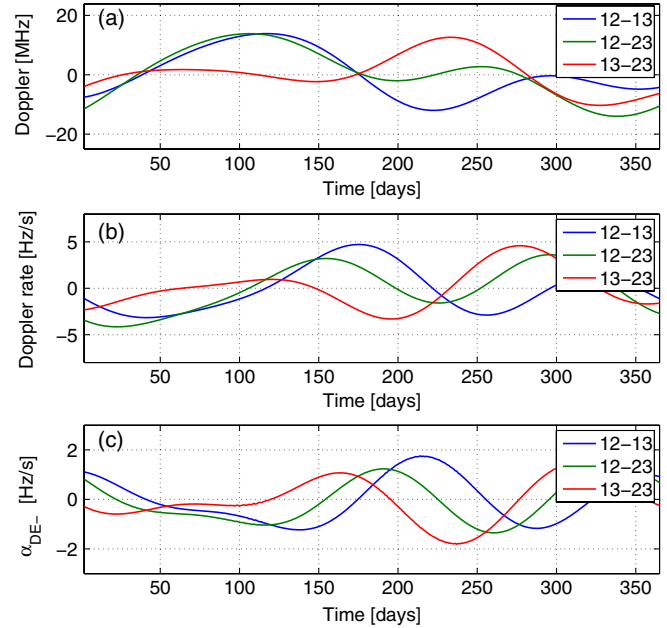

FIG. 36 (color online). (a) Difference Doppler frequency, (b) difference Doppler rate, and (c) 2nd time derivative of difference Doppler frequency for the different arm pairs.

[1] P. L. Bender, K. Danzmann, and the LISA Study Team, Max Plank Institute for Quantum Optics Report No. MPQ 233, 1998, http://www.srl.caltech.edu/lisa/documents/PrePhaseA.pdf.

[2] P. Gath, LISA Technical Report No. LISA-ASD-TN-2011, 2008 (unpublished).

[3] R. W. P. Drever, J. L. Hall, F. V. Kowalski, J. Hough, G. M. Ford, A. J. Munley, and H. Ward, Appl. Phys. B **31**, 97 (1983).

[4] J. I. Thorpe, K. Numata, and J. Livas, Opt. Express **16**, 15 980 (2008).

[5] G. Heinzel, C. Braxmaier, M. Caldwell, K. Danzmann, F. Draaisma, A. F. Garcia Marin, J. Hough, O. Jennrich, U. Johann, C. Killow, K. Middleton, M. te Plate, D. Robertson, A. Rudiger, R. Schilling, F. Steier, V. Wand, and H. Ward, Classical Quantum Gravity **22**, S149 (2005).

[6] B. S. Sheard, M. B. Gray, D. E. McClelland, and D. A. Shaddock, Phys. Lett. A **320**, 9 (2003).

[7] J. Sylvestre, Phys. Rev. D **70**, 102002 (2004).

[8] M. Tinto and M. Rakhmanov, arXiv:gr-qc/0408076v1.

[9] M. Tinto and J. W Armstrong, Phys. Rev. D **59**, 102003 (1999).

[10] J. W. Armstrong, F. B. Estabrook, and M. Tinto, Astrophys. J. **527**, 814 (1999).

[11] D. A. Shaddock, M. Tinto, F. B. Estabrook, and J. W. Armstrong, Phys. Rev. D **68**, 061303(R) (2003).

[12] A. F. Garcia Marin, G. Heinzel, R. Schilling, A. Rudiger, V. Wand, F. Steier, F. G. Cervantes, A. Weidner, O. Jennrich, F. J. Meca Meca, and K. Danzman, Classical Quantum Gravity **22**, S235 (2005).

[13] J. I. Thorpe and G. Mueller, Phys. Lett. A **342**, 199 (2005).

[14] B. S. Sheard, M. B. Gray, and D. E. McClelland, Appl. Opt. **45**, 8491 (2006).

[15] A. Sutton and D. A. Shaddock, Phys. Rev. D **78**, 082001 (2008).

[16] M. Herz, Opt. Eng. (Bellingham, Wash.) **44**, 090505 (2005).

[17] D. A. Shaddock, B. Ware, P. G. Halverson, R. E. Spero, and B. Klipstein, AIP Conf. Proc. **873**, 654 (2006).

[18] D. A. Shaddock, B. Ware, R. E. Spero, and M. Vallisneri, Phys. Rev. D **70**, 081101(R) (2004).

[19] M. Tinto, D. A. Shaddock, J. Sylvestre, and J. W. Armstrong, Phys. Rev. D **67**, 122003 (2003).

[20] G. Heinzel, C. Braxmaier, K. Danzmann, P. Gath, J. Hough, O. Jennrich, U. Johann, A. Rudiger, M. Sallusti, and H. Schulte, Classical Quantum Gravity **23**, S119 (2006).

[21] M. Tinto, F. B. Estabrook, and J. W. Armstrong, Phys. Rev. D **65**, 082003 (2002).

[22] M. Tinto, F. B. Estabrook, and J. W. Armstrong, Phys. Rev. D **69**, 082001 (2004).

[23] R. W. Hellings, G. Giampieri, L. Maleki, M. Tinto, K. Danzmann, J. Hough, and D. Robertson, Opt. Commun. **124**, 313 (1996).

[24] R. W. Hellings, Phys. Rev. D **64**, 022002 (2001).

[25] G. de Vine, D. A. Shaddock, R. E. Spero, B. Ware, K. McKenzie, and W. Klipstein (unpublished).

[26] P. Gath, LISA mission formulation technical Report No. LISA-ASD-TN-2004, 2006 (unpublished).

[27] V. Wand, Y. Yu, S. Mitryk, D. Sweeney, A. Preston, D. Tanner, G. Mueller, J. I. Thorpe, and J. Livas, J. Phys. Conf. Ser. **154**, 012024 (2009).

[28] LISA Frequency Control White Paper, LISA Frequency control study team, ESA document LISA-JPL-TN-823, 2009 (unpublished).

[29] P. Gath, LISA performance engineering technical note, LPE-ASD-TN-0005, 2009 (unpublished).

[30] Frequency control study team meeting, held at the California Institute of Technology, Pasadena, CA, October 2008.

[31] K. McKenzie and D. A. Shaddock, LISA Tech. Report No. LIMAS-2008-001, 2008 (unpublished).

[32] B. S. Sheard, A. F. Garcia Marin, F. Guzman, and G. Heinzel, Laser Frequency Prestabilisation for LISA, LTP-style Pre-stabilisation: Additional Comments, presentation to the frequency control study team meeting, 2008 (unpublished).

[33] http://www.mathworks.com/.

[34] P. Gath (private communication).